



Basinal Brines at the Origin of the Imiter Ag-Hg Deposit (Anti-Atlas, Morocco): Evidence from LA-ICP-MS Data on Fluid Inclusions, Halogen Signatures, and Stable Isotopes (H, C, O)

Samira Essarraj,^{1,†} Marie-Christine Boiron,² Michel Cathelineau,² Alexandre Tarantola,²
Mathieu Leisen,^{2,3} Philippe Boulvais,⁴ and Lhou Maacha⁵

¹Laboratoire Géoressources, URAC 42, Faculté des Sciences et Techniques, Université Cadi Ayyad, BP 549, Marrakesh, Morocco

²GeoRessources, CNRS, Université de Lorraine, CREGU, Faculté des Sciences, B.P. 70239, 54506, Vandoeuvre-lès-Nancy cedex, France

³Andean Geothermal Center of Excellence (CEGA), Universidad de Chile, Santiago, Chile

⁴Géosciences Rennes, UMR 6118, OSUR, Université de Rennes I, Campus de Beaulieu, 35042 Rennes Cedex, France

⁵MANAGEM Group, 191, bd Mohamed Zerkoutni, angle bd. Massira Alkhadra, Twin Center Tour A-20100 Casablanca, Morocco

Abstract

The Imiter Ag-Hg deposit is located in the Precambrian volcano-sedimentary formations of the Saghro inlier (eastern part of the Anti-Atlas Mountains, Morocco). The orebodies consist of northeast-southwest to east-west veins and lenses hosted by Cryogenian black shales and graywackes and Neoproterozoic conglomerates, and are controlled by an east-west fault network, the so-called Imiter fault. Mineralogical and paleo-fluid geochemistry investigations (microthermometry, Raman spectroscopy, LA-ICP-MS on individual inclusions, bulk crush-leach analyses, and stable isotope data (O, H)) show that the main Ag ore stage is related to circulation of deep-basinal sedimentary brines (Na-K-(Mg) (salinity = 16.7 to ≥ 26 wt % NaCl equiv, molar Cl/Br = 330, $\delta^{18}\text{O} = 2.15\text{--}2.35\text{‰}_{\text{SMOW}}$, and $\delta\text{D} = -53.8$ to $-65.5\text{‰}_{\text{SMOW}}$), at temperatures of about 180° to 220°C and hydrostatic pressures. The main driving mechanism for silver ore deposition is the dilution of ore-bearing brines by a low-salinity meteoric fluid containing a low-density volatile component ($\text{N}_2 > \text{CH}_4 > \text{CO}_2$), $T_{\text{H}} = 180^\circ$ to 220°C, $\delta^{18}\text{O} = -1.4\text{‰}_{\text{SMOW}}$, and δD of about $-28.2\text{‰}_{\text{SMOW}}$. Silver content of the brines ranges from 2 to 30 mmol/kg solution (up to 3,200 ppm Ag, avg Ag concentration about 900 ppm), whereas the maximum Ag content found in dilute waters is about 0.4 mmol/kg solution (40 ppm). The ore-forming model proposed for the Imiter deposit is (1) Ag extraction from the basement by the penetration of deep-basinal brines, and (2) deposition in a structural trap through fluid mixing with recharge fluids. This model is comparable to that described worldwide for the origin of Pb-Zn, F, Ba, and U deposits near unconformities between basement and sedimentary basins. Similarities among the major Ag deposits from the Anti-Atlas (Imiter, Zgounder, Bou Azzer) strongly suggest that they resulted from a unique event, likely related to the opening of the Atlantic Ocean. The silver ores are superimposed on the same lineament as a preexisting uneconomic Pan-African Co-Ni-As system linked to magmatic intrusions, but Ag ores have no genetic relationship with them.

Introduction

The Imiter deposit is a world-class Ag-Hg deposit located in the Precambrian basement of the Anti-Atlas belt (Morocco), which also hosts the Zgounder (Ag-(Hg)) and Bou Azzer (Co-(As-Ag-Au)) deposits, among others (Fig. 1). Several authors considered the Moroccan Ag-(Co-As) deposits as synchronous with the major metamorphic stages of Pan-African age (dated at 685 Ma, Rb/Sr on clay minerals, Clauer, 1976) at Bou Azzer (Leblanc and Lbouabi, 1988), or with the magmatic intrusions at Imiter (550 \pm 3 Ma, U/Pb on rhyolite zircon, Levresse, 2001; Levresse et al., 2004; and Ar/Ar on muscovite, Cheilletz et al., 2002). No direct dating of the ores exists. Hypothetical Neoproterozoic ages consistent with the conceptual genetic models (metamorphic or magmatic-hydrothermal) were thus proposed. Levresse (2001) interpreted the Ag-Hg ores as having formed within the context of a neutral epithermal model related to a north-south extensional tectonic setting that provided traps for the injection of rhyolitic magmas near the Precambrian-Cambrian transition, and the synchronous concentration and deposition of metals.

Based on structural and mineralogical investigations, Tuduri et al. (2005) proposed a three-stage model for the formation of the mineralized veins at Imiter to explain the structural controls and vein formation. The first stage involves WNW-ESE shortening corresponding to a dextral transpressive event, responsible for the formation of quartz-(pink dolomite) and Ag-rich structures. The second stage is associated with a normal left-lateral motion controlled by north-south shortening that reopened previous structures filled only by barren pink dolomite. The last stage corresponds to weathering leading to Ag enrichment in the quartz-carbonate veins. Tuduri et al. (2005) did not attribute a specific age to these stages of deformation.

No detailed determination of the ore fluid chemistry in relationship to metal deposition exists and numerous studies question magmatic Neoproterozoic models of Ag deposition at Imiter (Essarraj et al., 2005; Borisenko et al., 2014). The present study focuses on the paragenetic sequence of Ag ores with the successive stages of fluid circulation in order to determine the physical and chemical properties and origin of the ore fluids as well as the mechanisms that control Ag ore formation. Special attention was paid to the fluid chemistry changes responsible for Ag deposition. Microthermometry

[†]Corresponding author: e-mail address, s.essarraj@uca.ac.ma

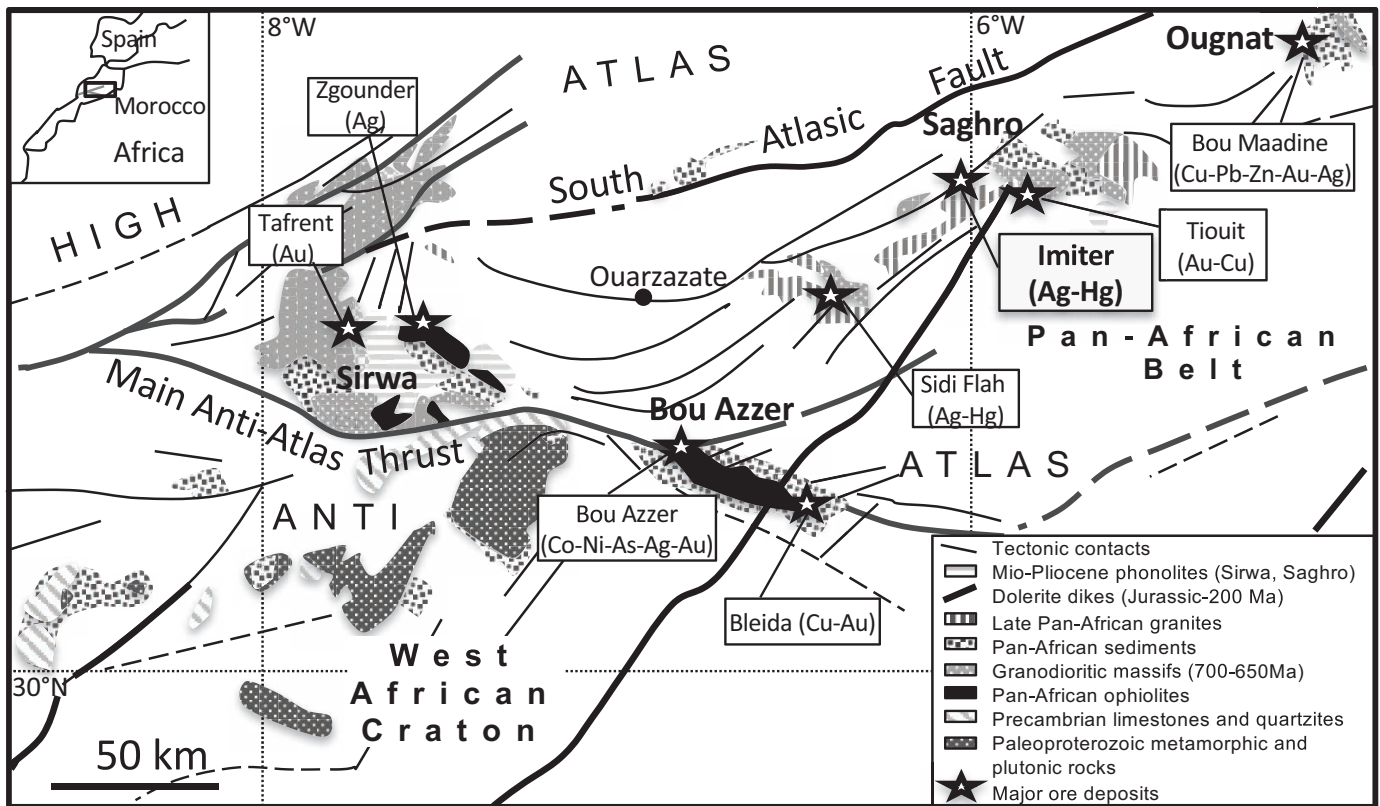


Fig. 1. Geologic sketch map of the Anti-Atlas and location of the major Ag deposits (among others) in the Pan-African belt (modified from Bousquet et al., 2008).

and Raman spectroscopy (used for salinity, temperature, and gas content determinations), and laser-ablation-inductively coupled plasma-mass spectrometry (LA-ICP-MS) (for major cations, and metal content quantification) were used on individual inclusions and a bulk-leachate analysis (halogen content determination) was carried out in order to understand the significance of the main fluid events responsible for the genesis of the Imiter deposit. Special attention has been paid to the analysis of Ag concentration in fluid inclusion by LA-ICPMS. Oxygen, carbon, and hydrogen isotope signatures of the fluid inclusions and halogen ratios were investigated to infer the sources of fluids. In this paper, we propose a new model of fluid circulation and Ag deposition at Imiter that implies circulation of basinal brines during or after the Triassic. We discuss this model at the scale of the central and eastern Anti-Atlas belt.

Geologic Setting

Regional geology

The Imiter Ag-Hg deposit is located approximately 150 km east of Ouarzazate (Morocco), in the Precambrian formations of the Saghro inlier (eastern part of the Anti-Atlas Mountains). The deposit was exploited from the 8th until the 13th century. Present exploitation began in 1969 by the SMI Company (MANAGEM group) and continues to the present day; the average exploitation rate is close to 250 t/yr Ag.

The Saghro inlier is a part of the 680 to 580 Ma Pan-African orogenic belt (Fig. 1). It is located north of the main Anti-Atlas

thrust, which is a major E-W-trending fault zone constituting the northern boundary of the West African craton (Fig. 1) with an age of 2.2 to 1.7 Ga (Eburnean orogeny; U/Pb on zircon, Aït Malek et al., 1998; Thomas et al., 2002). The Pan-African orogeny started by rifting and the formation of an ophiolitic complex during the Middle Precambrian (Early Neoproterozoic, called PII locally), around 788 ± 9 Ma (Rb/Sr on clay fractions, Clauer, 1976). Two tectonic phases are distinguished—a first and major B1 phase, dated at 685 ± 15 Ma (Rb/Sr on metamorphic illite, Clauer, 1976), and a second phase B2, dated at 623 ± 18 Ma (Rb/Sr on clay minerals, Clauer, 1976) and 615 ± 12 Ma (U/Pb on zircon, Ducrot, 1979). Significant magmatic activity is recognized in the Saghro area and corresponds to a postcollisional calc-alkaline magmatism around 620 to 608 Ma (Inglis et al., 2004). A back-arc basin formed and was first filled by a synorogenic volcano-sedimentary series in the Early Neoproterozoic (Cryogenian or PII), and then by Ouarzazate volcano-sedimentary formations during the end of the Upper Neoproterozoic (Ediacaran or PIII; Fig. 2). The Late Neoproterozoic andesitic and ignimbritic magmatism and granodiorite intrusions belong to the Ouarzazate Formation.

At the end of the Precambrian, Adoudounian marine sediments including basal conglomerates and lower carbonates were deposited unconformably at an age estimated to be close to 534 ± 10 Ma, based on the U/Pb zircon ages obtained for the Jbel Boho volcano, considered as synchronous with sedimentation (Ducrot and Lancelot, 1977). The Anti-Atlas Paleozoic cover series were dominantly deposited in a shallow marine environment and show a layer cake configuration with

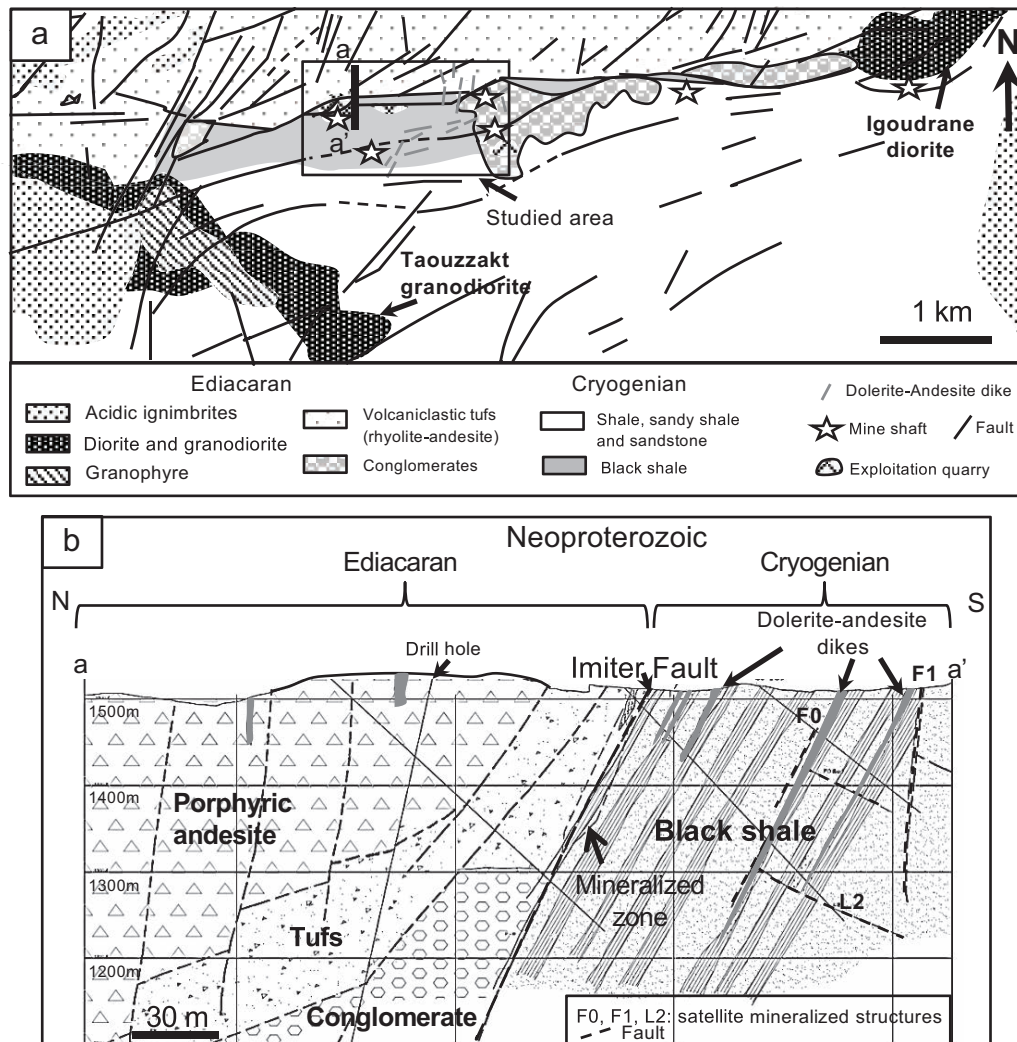


Fig. 2. (a). Local geology of the Imiter mine, from Tuduri et al., (2005) and SMI documents. (b). North-south geologic section on the Imiter mine (a-a' bold line in the studied area, SMI document).

a thickness reaching 6 to 10 km from east to west of the Anti-Atlas (Burkhard et al., 2006).

During closure of the Rheic Ocean, the collision between Laurentia and Gondwana induced the deformation of the basin (Secor et al., 1986). This Variscan event led to the inversion of the normal faults, basement uplift, and folding of the covering rocks (Robert-Charrie and Burkhard, 2008). A new extensional stage affected the central and eastern Anti-Atlas during the Atlantic opening in the Mesozoic (Burkhard et al., 2006). During the Late Triassic and Early Liassic, clastic and evaporitic sequences were deposited in several Atlantic basins around the Anti-Atlas, mainly to the north of the study area (Poisson et al., 1998; El Arabi, 2007). Based on apatite fission tracks from both the central and western Anti-Atlas inlier, Oukassou et al. (2010) established that the final exhumation of the Anti-Atlas took place during the Neogene, i.e., synchronous with the High Atlas exhumation.

Local geology

The Imiter deposit is located in the northern part of the Jbel Saghro and consists of volcano-sedimentary formations (1,200

m thick) of Cryogenian (or PII) age. The black shales and gray-wackes hosting Ag ores (Ouguir et al., 1996) are the upper formations of the Cryogenian series forming the Saghro Group in this part (Fig. 2) and are considered to have been deposited in a back-arc context (Ouguir et al., 1996). These series were deformed during B1 and B2 tectonic phases (schistosity, folding). Silver ores are also observed within detrital formations (basal conglomerates) from Ediacaran rocks. In the Imiter area, Cryogenian volcano-sedimentary formations are intruded by Igoudrane and Taouzzakt granodiorites (dated at 572 ± 5 Ma by U/Pb dating of zircon for Taouzzakt, Cheilletz et al., 2002), which developed a contact metamorphism. These granodiorites have similar ages to the Askawn granodiorite from the Zgouder area (U/Pb dating of zircon at 575 ± 8 Ma, Thomas et al., 2002) and the quartz-diorites of Bou Azzer (Leblanc, 1972).

According to Benharref (1991), Late Neoproterozoic volcanic activity is observed in the Saghro area and is sometimes controlled by large regional fractures. At Imiter, the Takhatert rhyolitic dome was dated at 550 ± 3 Ma (U/Pb on zircon, Cheilletz et al., 2002), and several rhyolitic dikes emplaced in

east-west normal faults at 543 ± 9 Ma (U/Pb dating of zircon, Gasquet et al., 2005).

The orebodies of the Imiter deposit are northeast-southwest to east-west lenses and vein networks, measuring several millimeters to centimeters in width and meters in length, hosted by Cryogenian black shales and graywackes as well as Ediacaran basal conglomerates (Fig. 2). The Imiter fault system consists of a complex association of discontinuities striking N 90°E and N 60°–70°E for almost 10 km (Leistel and Qadrouci, 1991; Ouguir et al., 1994). This fracture network shows a succession of apparent pull-apart geometries at the map and mine work scales (Ouguir et al., 1994; Tuduri et al., 2005). It results from a north-south distensive deformation phase leading to the development of northwest-southeast sinistral distensive strike-slip faults (Ouguir et al., 1994).

The Ag-Hg orebodies at Imiter are predominantly quartz-dolomite veins and veinlets with a very high average Ag grade of 700 to 800 g/t Ag. The estimated production is 4,300 t Ag for the 1960 to 2011 period and the total reserves are approximately 3, 965 Mt Ag (MANAGEM company report, 2015, <http://www.managemgroup.com/Media-Center>).

Methods

Fluid inclusions

The fluid inclusion classification follows the convention of Boiron et al. (1992). It is based on the mode (dew or bubble transition, V or L) of total homogenization and the fluid components (subscript c for carbonic species (CO₂/CH₄), n for N₂, and w for water). The subscripts are ordered according to the relative abundance of the various species in the fluid.

Bulk composition and density: Fluid inclusions were studied by microthermometry on doubly polished wafers, using a Chaix-Meca heating-freezing stage (Poty et al., 1976), and a Linkam THSMG600 freezing-heating stage (Shepherd, 1981). For the microthermometric data, the following abbreviations are used: T_{m(CO₂)} = melting temperature of the volatile phase, T_{h(CO₂)} = homogenization temperature of the volatile phase, T_e = eutectic or apparent eutectic temperature, the temperature at which the first droplets of liquid are observed during low-temperature experiments, T_{m(hh)} = final melting temperature of hydrohalite, T_{m(ice)} = final melting temperature of ice, T_{m(cl)} = melting temperature of clathrate, and T_{h(L or V)} = total homogenization temperature (L + V to liquid or L + V to vapor, respectively). For most of the aqueous fluid inclusions, salinity calculations were carried out in the H₂O-NaCl system using the data from Bodnar (1993). When T_{m(hh)} values were recorded, salinity calculations were made in the H₂O-NaCl-CaCl₂ system using data from Steele-MacInnis et al. (2011). Molar fractions of CO₂, CH₄, and N₂ in the volatile phase were determined in individual inclusions by micro-Raman analysis performed on a DILOR LABRAM Raman spectrometer at the GeoRessources laboratory (Nancy, France). The bulk composition, molar volume, volatile/water ratio, and salinity were calculated from the *P-V-T-X* properties of individual carbonic inclusions in the C-O-H-S system (Dubessy, 1984; Dubessy et al., 1989; Thiery et al., 1994; Bakker, 1997). Isochores were calculated using the program ISOC from the computer package FLUIDS-1 (Bakker, 2003) based on data from Bowers and Helgeson (1983).

Bulk crush-leach analyses were performed on quartz and dolomite samples devoid of mineral inclusions. Samples were prepared and cleaned using the method explained in Banks and Yardley (1992). Analyses of the halogens Cl, Br, and SO₄ were carried out by ion chromatography on doubly distilled water leachates.

Determination of Ag and trace element content in fluid inclusions using LA-ICP-MS: LA-ICP-MS analyses were carried out on individual fluid inclusions in order to determine the concentration of major and trace elements (metals, in particular) in the fluids related to Ag deposition. The LA-ICP-MS instrument (GeoRessources laboratory, Nancy, France) comprises a GeoLas excimer laser (ArF, 193 nm, Microlas, Göttingen, Germany; Günther et al., 1997) and an Agilent 7500c quadrupole ICP-MS, equipped with an octopole reaction cell using H₂ gas, and a collision cell using He gas. The laser beam is focused onto the sample within an ablation cell with a Schwarzschild objective (magnification ×25) linked to a CCD camera. The ablation chamber is cylindrical and has a volume equal to 24.5 cm³. Helium is used as a carrier gas to transport the ablated material (Günther and Heinrich, 1999). The He flow for all of the samples was close to 0.5 l/min. The aerosol of the ablated material is mixed with Ar via a cyclone mixer (vol 9.5 cm³) before its introduction into the ICP plasma torch for optimal ionization. Analyses were carried out without using the collision-reaction cell. The signal of the matrix near the fluid inclusions is used to quantify the background and to correct the signal intensity for each element (Leisen et al., 2012a). Elements were considered as detected only when the magnitude of the LA-ICP-MS signal was more than three times the standard deviation of the background (Longerich et al., 1996).

Results for the analyzed elements were quantified using the NIST SRM 610, 612, 614 (Pearce et al., 1997) as external standards. Calibration curves relative to sodium for Mg, K, Ca, Fe, Mn, Ag, Cu, Zn, Sr, Ba, and Pb were established. In addition, to validate the Ag analyses on the fluid inclusions, aqueous NaCl solutions were prepared with various Ag concentrations and loaded in silica glass capillaries. The Ag/Na ratios obtained by LA-ICP-MS analysis were calculated using NIST as external standards. A comparison with the initial Ag concentrations known for each solution shows the validity of the Ag analysis on the fluids. The detection limit for Ag is within the range of 0.5 to 1 ppm depending on the analyzed inclusion size. The calculation method for the chemical composition of the fluid inclusions is based on a combination of the ice-melting temperature, a Pitzer-based thermodynamic model, and the LA-ICP-MS Na/cation ratios according to Leisen et al. (2012a).

It was not possible to perform an in situ determination of the Cl and Br contents, following the procedure described by Leisen et al. (2012b), due to the small size of the Imiter fluid inclusions (<20 μm).

Isotope geochemistry

Stable isotope analyses, including δ¹⁸O values of quartz and both δ¹⁸O and δ¹³C values of dolomite, were carried out at the stable isotope laboratory at Geosciences Rennes (University of Rennes 1, France). Millimeter crystals of quartz and dolomite were extracted manually and the mineral purity was

assessed under a binocular microscope. Dolomite crystals were crushed before the reaction with anhydrous orthophosphoric acid at 50°C. Stable isotope analyses were performed on CO₂ with a VG SIRA 10 triple-collector instrument at the University of Rennes 1. The isotopic compositions are given using the δ notation relative to V-SMOW (O) and V-PDB (C). Using internal carbonate standards, the reference material NBS 19 as well as replicate analyses of the samples, the reproducibility of the C and O analyses was better than $\pm 0.1\%$. The quartz was also hand-picked and its ¹⁸O/¹⁶O ratio was measured on the oxygen liberated using the conventional fluorination method of Clayton and Mayeda (1963) and then converted to CO₂ by reaction with hot graphite. The uncertainty (estimated from duplicates performed on different Ni fluorination tubes) is generally on the order of 0.1‰.

The δ D analysis of fluids from fluid inclusions was performed at the Centre de Recherches Pétrographiques et Géochimiques (CRPG) laboratory (Nancy, France). Quartz and dolomite crystals were weighed (454–1,135 mg) and put in steel tubes. Mineral-bearing tubes were connected to a vacuum extraction line and heated overnight at 120°C to release H₂O adsorbed at the mineral surface (Dublyansky and Spötl, 2009). Preliminary microthermometric tests showed that fluid inclusions did not decrepitate or stretch at temperatures below 200°C. The mineral-bearing tubes were subsequently crushed under vacuum to release fluids hosted in the quartz grains. Water was trapped under vacuum in a liquid nitrogen-cooled U-shaped tube. Noncondensable gases and CO₂ were removed from the extraction line. Water was reduced to H₂ by passing through a uranium reactor heated to 800°C. Hydrogen gas was trapped in glass tubes and analyzed using a VG 602D mass spectrometer at the CRPG laboratory (Nancy, France). All of the results are expressed with respect to V-SMOW. Two laboratory internal standards were analyzed weekly to optimize the accuracy of the isotopic measurements. There may be a bias in the δ D values from the memory effect within the uranium reactor. In order to avoid this issue, samples were systematically duplicated, and the δ D deviance between each isotopic measurement was less than $\pm 1.5\%$. For each duplicate, the δ D values from the first extraction were therefore considered as not having been potentially affected by this memory effect. Taking the overall reproducibility of the internal standards and sample duplicates into account, the accuracy of the D/H measurements is within 3‰.

Ore Mineralogy and Paragenesis

A paragenetic sequence for Imiter is given in Figure 3 and includes the uneconomic Ni-Co-As stage and the main (Pb-Zn)-Ag ore stages. The Ag ores are presented in Figure 4 and the quartz-carbonate ore veins in Figure 5a and b.

Ni-Co-As stage

The early hydrothermal stages are characterized by the formation of quartz, pyrite, and Fe (Ni-Co) sulfarsenides. First, coarse-grained milky quartz (QI) filled irregular millimeter-to centimeter-scale veinlets crosscutting or brecciating the host rocks. Ductile deformation produced high deformation and boudinage of the QI veins, with the formation of small newly formed microcrystalline quartz microdomains (criteria from Tullis et al., 1973; Bowler, 1989; Fig. 5c).

This first generation of quartz (QI) underwent numerous microfracturing stages resulting in fluid inclusion planes (FIP) with various orientations. Abundant scattered fluid inclusions and a high-density FIP network resulted in the cloudy appearance of QI (Fig. 5d). QI hosts synchronous pyrite I, arsenopyrite I (Fig. 6a), and pyrrhotite, as well as some muscovite platelets, and rare dolomite I grains. Pyrite, arsenopyrite, and pyrrhotite are strongly deformed and corroded. Pyrite I and pyrrhotite form bands, 100 to 200 100–200 μ m in width, in the black shale parallel to the ore veins. Pyrite I, arsenopyrite I, and Ti oxides are also observed as disseminated grains in the black shale. Cobalt-nickel-sulfarsenide (Co-rich gersdorffite) was probably formed later than QI-pyrite I and is strongly corroded and partially replaced by minerals such as sphalerite, galena, and Ag minerals from later stages (Fig. 6b).

A second generation of early quartz, designated QII (Fig. 5c, d), occurs as veinlets of coarse-grained to microcrystalline hyaline quartz. This QII hosts a second generation of euhedral pyrite (pyrite II, Fig. 6c), which occurs as crystals of variable size, sometimes centimeter scale and often microfractured, as well as euhedral arsenopyrite II (50–400 μ m in width, Fig. 6d). Arsenopyrite II crystals contain Se and Co as trace elements and are associated with Ni cobaltite (with traces of Fe) euhedral crystals and Co arsenide (alloclasite) (Fig. 7a). A first generation of deformed galena with curved cleavage planes (Fig. 6e) is found with QI or QII, but no clear genetic relationships were established between galena and these quartz generations. Magnesium-rich chlorite (Si_{2.88} AlIV_{1.12}) (AlVI_{1.35} Fe_{2.43} Mg_{2.08} Mn_{0.03}) O₁₀ (OH)₈ (on the basis of 14 atoms of oxygen) crystallized at the edges of QII (Fig. 8c).

(Pb-Zn)-Ag ore stages

Two successive Pb-Zn-Ag ore-bearing events were distinguished (Fig. 3)—a base metal stage and an Ag stage.

Base metal stage: Quartz (QIII) veins and veinlets are characterized by growth zones and show mosaic and comb textures (Fig. 5e, f). In several zones, the quartz comb crystals show feathery and undulose extinction, and frequently grow on microcrystalline QII. Rhombic comb euhedral fine-grained adularia (<50 μ m) constitutes the first mineral to form in the QIII comb veins. Small amounts of dolomite (dolII) are associated with QIII (QIII-dolII intergrowth and both are crosscut by late dolomite). Dark brown sphalerite I (Fig. 6g, i) and galena are associated with the QIII crystals (sometimes inclusions of sphalerite and galena are found in the QIII crystals) and occur as fracture infillings and corroded early sulfides. Small amounts of chalcopyrite were deposited at the end of this stage (Fig. 6g).

Ag stage: Hyaline geodic quartz QIV (Figs. 4a, b, 5e-g) grows on the QIII crystal rims and forms veinlets measuring several micrometers to millimeters in width. A succession of carbonates crystallized after all of the quartz generations as follows: pink dolomite (dolIII) is observed in the core of the QIII-QIV veinlets (Fig. 5a, b, g) and as large infillings linked to the reactivation of the Imiter fault network throughout the deposit; the dolIII veinlets crosscut and offset the QIII veins and QIV crystals; calcite veins are barren and observed in several parts of the deposit as crosscutting dolIII veins and as late infillings in unfilled geodes of dolIII (Fig. 5b); and finally, ankerite veins (μ m to mm) are observed in the entire deposit

Minerals	Ni-Co-As stage	Ag ore stages		
Pyrite I	—————			
Pyrrhotite	—————			
Arsenopyrite I	—————			
Co-Ni-sulfarsenide	—————			
Pyrite II	—————			
Arsenopyrite II	—————			
Cobaltite (Ni)	—————			
Co-arsenide	—————	I		II
Sphalerite		—————		—————
Chalcopyrite		—————		—————
Galena	————— ?	—————		—————
Imiterite		—————		—————
Pearceite-Polybasite		—————		—————
Ag-Cu sulfide (Mckinstryite)		—————		
Pyrargyrite				—————
Native Ag		—————		—————
Sternbergite		—————		—————
Ag-Hg		—————		—————
Acanthite		—————		—————
Quartz QI	—————			
Muscovite	—————	II		III
Dolomite	————— I	—————		—————
Chlorite	—————			
Quartz QII	—————			
Adularia		—————		
Quartz QIII		—————		
Quartz QIV		—————		
Calcite				—————
Ankerite				—————
Fluid inclusion types				
Vc-w, Lc, Lc-w, Lw-c	—————			
Lw		Lw1	Lw2/Lw2b	Lw3
Tectonic stages	A	B	C	
A: NNW-SSE à N-S extensive phase B: NW-SE to WNW-ESE shortening → dextral-reverse transpressive event C: N-S shortening → normal left-lateral/sinistral motion				

Fig. 3. Paragenetic sequence of the Imiter deposit, associated fluid types, and deformation phases (a), (b), and (c). Tectonic events: (a). From Ouguir et al. (1994) and Levresse (2001). (b) and (c). From Tuduri et al. (2005). See the text for the definition of the fluid-type abbreviations.

and crosscut both the early and later quartz, and all of the dolomite generations (Fig. 7f, g).

The Ag minerals and associated sulfides (Figs. 3–7) are deposited during two episodes. The first and main Ag stage (Figs. 5–7) is synchronous with QIV and is characterized by the following mineral association—imiterite, an Ag-Hg sulfide that is abundant and often fractured and brecciated, accompanied by a small amount of galena (Fig. 6f, j, k); Ag sulfosalts (pearceite-polybasite) that are sometimes corroded and replaced by late galena (Fig. 7b); and a rare Ag-Cu sulfide ($\text{Ag}_{5.1}\text{Cu}_{2.9}\text{S}_4$ reaching mckinstryite's ideal formula $\text{Ag}_5\text{Cu}_3\text{S}_4$). Acanthite, native Ag, Ag-Hg amalgam, and sternbergite (Ag-Fe sulfide, with small amounts of Hg) exhibit a mirmekitic texture with Ag-Hg amalgam that formed later on. The QIII

and QIV veins and microdomains host most of the Ag minerals probably because of their high porosity (abundance of voids and geodes).

The second Ag stage postdates the QIV and dolomite III deposition and is characterized by the formation of acanthite and polybasite-pearceite, both of which cement brecciated imiterite. Pyrargyrite, Ag-Hg, and Ag galena formed during this stage. Acanthite, Ag-Hg amalgam, and galena are closely associated with the ankerite and are mainly observed on microfractures that crosscut dolomite III (Fig. 7e-g). Sternbergite synchronous with Ag-Hg is postdated by Ag minerals and galena from the second stage (Fig. 7d).

Clear brown sphalerite (sphalerite II) and relatively scarce crystals of chalcopyrite were observed in the late carbonate

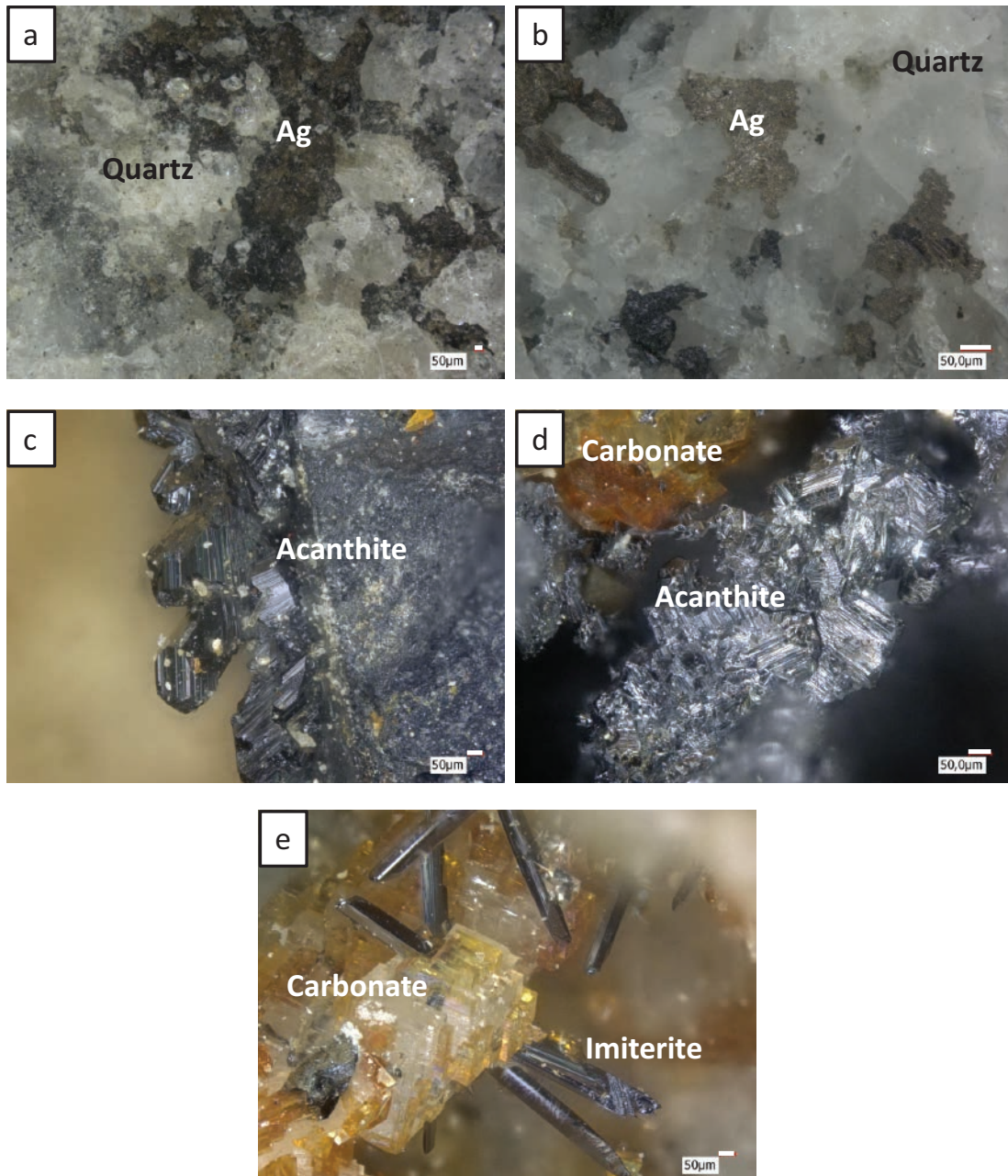


Fig. 4. Ag ores from the Imiter deposit. (a) and (b). Native Ag/Ag-Hg and associated quartz (QIII and QIV). (c), (d), and (e). Euhedral acanthite, imiterite, and late carbonate.

veins (dolomite III, calcite). Large amounts of galena fill the dolomite III geodes. Sphalerite II was observed in association with Ag in one microfissure.

Silver minerals and galena crystallized on the corrosion zones and fractures of early sulfides and sulfosalts (mainly pyrite, pyrrothite, arsenopyrite II, and Co-Ni sulfarsenides), and sometimes over sphalerite I and chalcopryrite crystals from the major base metal stage. In particular, Ag and Ag-Hg precipitated onto corroded and fractured arsenopyrite crystals, which acted as preferential nucleation centers as described by Knipe et al. (1991, 1992) for other precious metal deposits. In the black shale, Ag minerals are present as disseminations or

as millimeter-scale microfracture infillings, and also grew over the early pyrite bands.

Fluid Inclusion Chemistry

Microthermometric and Raman data

Fluid inclusions (FI) were studied mainly on clusters and healed microfractures (FIP) in quartz QI and QII for the characterization of the preore stage fluids, and in QIII and QIV for the ore fluids. In addition, FI in sphalerite I and II, and when possible in dolomite III, were studied. The different fluid generations and their relative chronology were determined for each fluid

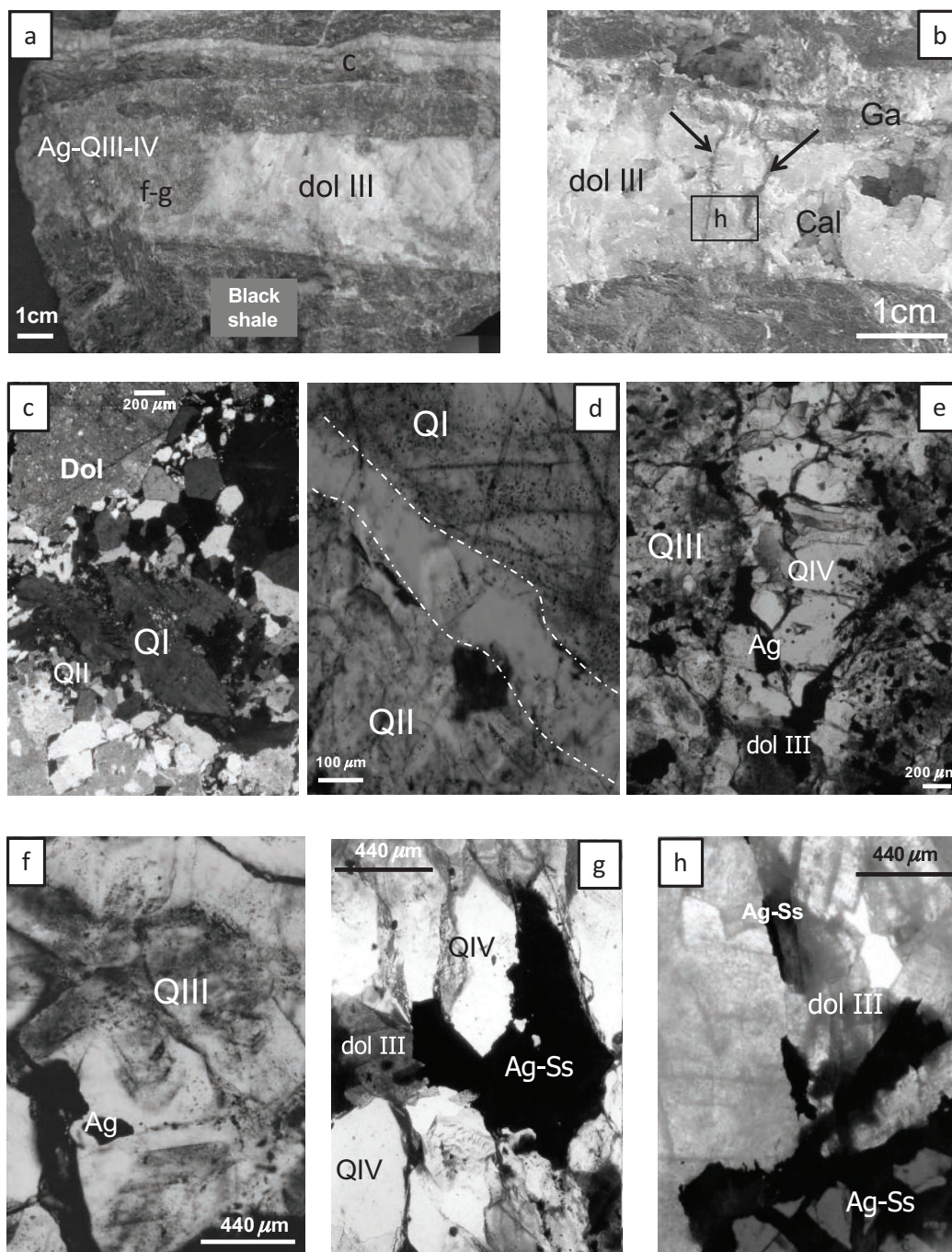


Fig. 5. Gangue minerals from the Imiter deposit. (a) and (b). Hand-picked specimens from the Imiter Ag mineralized quartz-dolomite veins. (c), (f), (g), and (h) correspond to the emplacements of the following microphotographs—(b) the arrows indicate late Ag fissures crosscutting the dolomite; the dolomite shows geodes filled by calcite (cal) and galena (Ga). (c), (d), (e), (f), (g), and (h). Microscopic observation on transmitted light. (c) and (d). Quartz QI and QII from early stages and dolomite (Dol). (e), (f), and (g). Late quartz from the base metal and Ag stages (zoned QIII) and hyaline QIV, respectively, late dolomite (dolIII) crystallizes at the core of the QIV vein. (h). Late Ag minerals (Ag-Ss = Ag sulfosalts) in geodes and fractures of dolomite III.

type according to the fluid inclusion petrography and textural relationships with the host mineral. Microthermometric data and Raman spectroscopy analyses are summarized in Table 1.

Ni-Co-As: One- and two-phase FI (Vc-w, Lc-w, Lw-c, Lc) are found as primary and secondary FI in QI and often as primary fluid inclusions in QII (Fig. 8, Table 1).

The Vc-w FI type is very abundant and consists of two-phase fluid inclusions at room temperature (<15 μm , 40 vol % H_2O , Fig. 8). The $T_{\text{m}(\text{CO}_2)}$ values range from -64.2° to -58.2°C , $T_{\text{m}(\text{cl})}$ from 3.5° to 15.1°C , and $T_{\text{h}(\text{CO}_2)}$ from -23.2° to 11.7°C to the carbonic liquid or vapor phase. The T_{h} values, measured by the disappearance of the aqueous

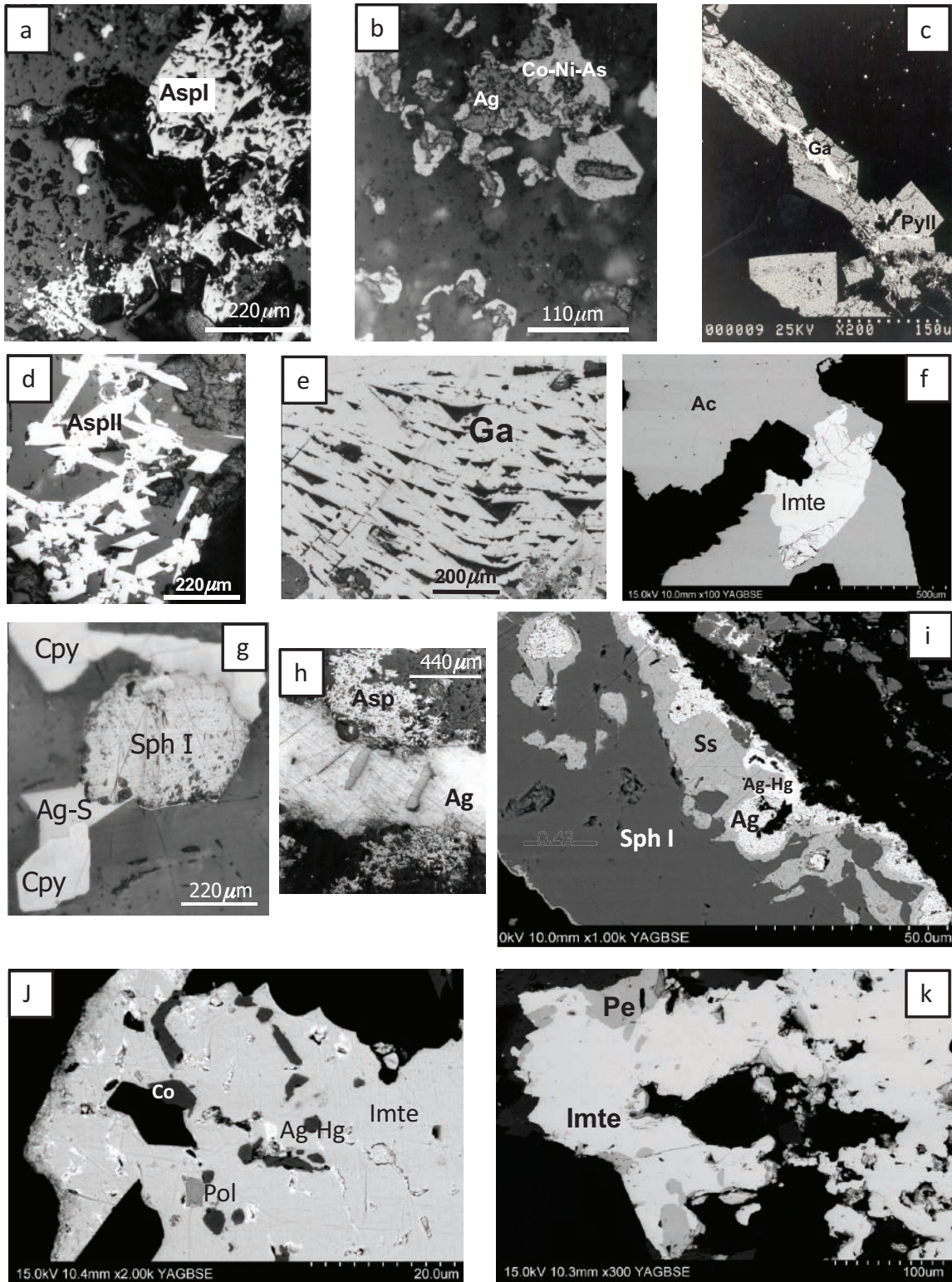


Fig. 6. Ore minerals from the Imiter deposit observed by reflected light microscopy (a), (b), (d), (e), (g), and (h) and by backscattered electron imaging (SEM) (c), (f), (i), (j), and (k). Early stages: (a) strongly corroded early arsenopyrite (AspI); (b) corroded early Co-Ni sulfarsenide (Co-Ni-As) invaded by Ag minerals (Ag); (c) euhedral pyrite II (PyII) with microfractures filled by late galena (Ga); (d) euhedral arsenopyrite II (AspII), (e) galena (Ga) with curved cleavage planes. Ore stages: (f) fractured imiterite (imte) and late acanthite (Ac); (g) sphalerite I (Sph I) and chalcocopyrite (Cpy) from the first base metal stage and Ag sulfide (Ag-S); (h) native Ag (Ag) crosscutting the early arsenopyrite (Asp); (i) sphalerite I (Sph I) followed by Ag mineral deposition (Ag = native Ag, Ag-Hg = Ag-Hg amalgam, Ss = Ag sulfosalt); (j and k) Ag minerals (imte = imiterite, Pe = pearceite, Pol = polybasite, Co = Fe-Ni cobaltite from early stages).

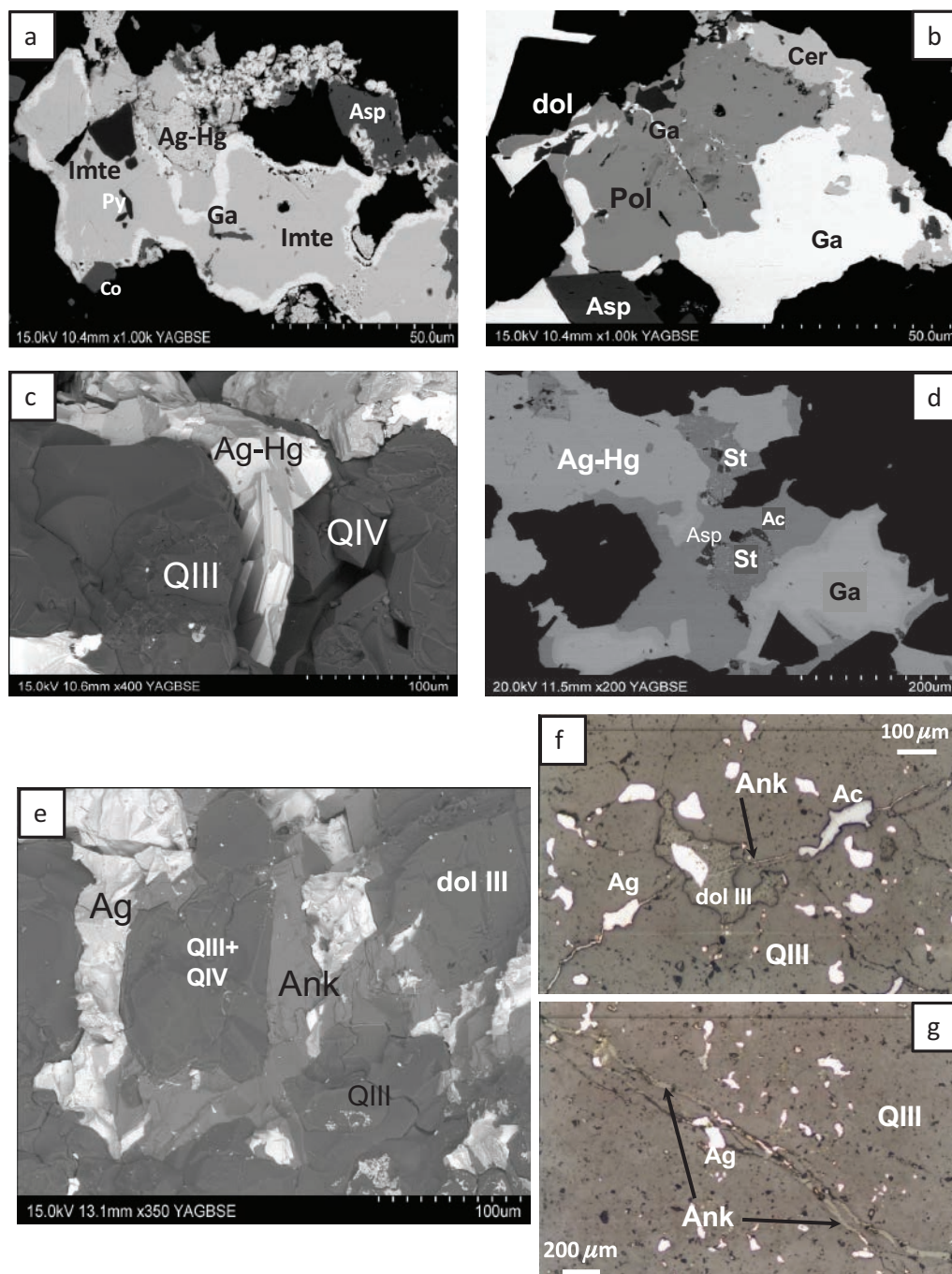


Fig. 7. Ore minerals from the Imiter deposit (continued) observed by scanning electron microscope (a), (b), and (d) backscattered electron imaging, (c) and (e) secondary electron imaging) and by reflected light microscopy (f) and (g). (a). Arsenopyrite II (Asp) and pyrite (py) from early stage and Ag minerals (Imte = imiterite and Ag-Hg amalgam) and associated galena (Ga). (b). Euheedral arsenopyrite II (Asp) from early stage and polybasite (Pol) (major Ag stage) with a fissure filled by galena (Ga) altered in cerusite (Cer). (c). Ag-Hg amalgam filling geode of QIII-QIV quartz. (d). Ag paragenesis with sternbergite (St), acanthite (Ac), Ag-Hg amalgam, and galena (Ga); (e), (f), and (g). Late Ag stage (native Ag and acanthite (ac)) associated with ankerite (Ank) (arrows) and postdating QIII, QIV, and dolomite III (dolIII): filling microfractures in quartz QIII, QIV, and dolomite III.

phase (LwLc->Lc or LwVc->Vc), range from 284° to 410°C. The volatile phase is dominated by CO₂ and CH₄. Nitrogen is a minor phase and small amounts of H₂S were detected in some fluid inclusions (Table 1). The salinity calculated from microthermometric data (T_{m(cl)}) and the volatile composition

determined by Raman analysis is within the range of 1 to 3 wt % NaCl equiv.

At room temperature, the Lc FI type occurs as abundant single-phase FI that are generally below 10 μm. The Lc FI are dominated by CO₂ and no visible water was observed

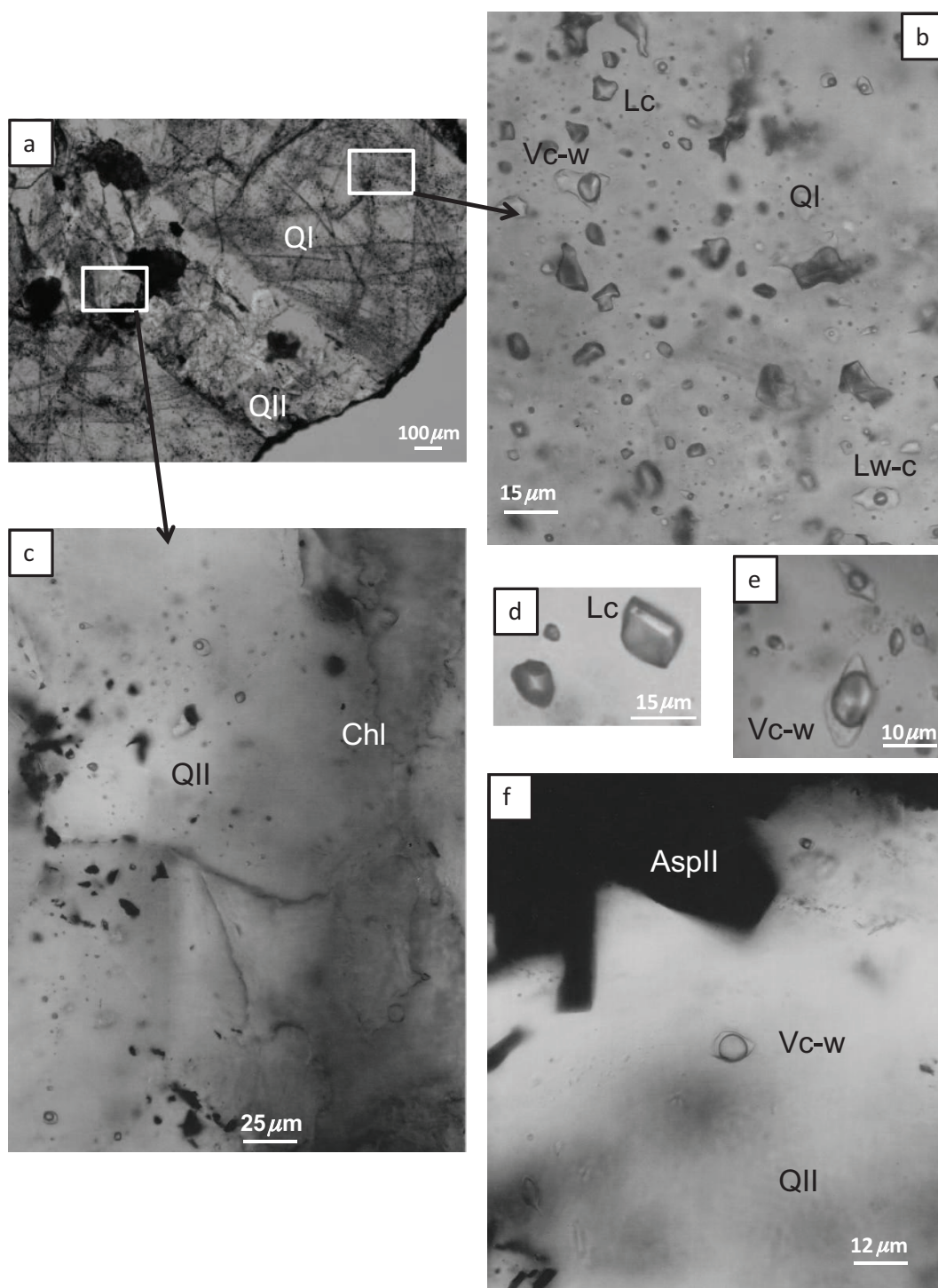


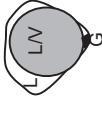










Fig. 8. Fluid inclusion types from the early stages. (a). Early quartz QI and QII. (b). Vc-w inclusions coexisting with Lc and Lw-c inclusions in QI. (c). Fluid inclusions in QII and associated chlorite (Chl). (d). Lc fluid inclusions with graphite solid. (e) and (f). Vc-w inclusions in QII quartz and associated euhedral arsenopyrite II (AspII). A detailed description of each fluid inclusion generation is given in the text.

(Fig. 8). The $T_{m(\text{CO}_2)}$ values are within the -61.8° to -59.8°C range, and $T_{h(\text{CO}_2)}$ is within the -17.5° to $+0.6^\circ\text{C}$ range (to the carbonic liquid phase, Table 1). High-density Lc FI are relatively scarce and are characterized by $T_{h(\text{CO}_2)}$ values between -56.4° and -40.4°C to the liquid phase. The Lc FI

are dominated by CO_2 and contain variable amounts of CH_4 and N_2 (Table 1).

Scarce Lc-w FI, containing around 60 to 70 vol % H_2O , are observed in microdomains dominated by Vc-w and Lc inclusions. For Lc-w FI, the $T_{m(\text{CO}_2)}$ values range from -61.5° to

Table 1. Summary of the Microthermometric Data for the Different Fluid Inclusion Types Observed at the Imiter Silver Deposit, Corresponding Salinities and Chemical Composition of Volatile Fluid Inclusions Obtained by Raman Microprobe Analysis

Fluid inclusion types	Microthermometry							Salinity		Raman data (Volatile phase)
	$T_{m(CO_2)}$ (°C)	$T_{h(CO_2)}$ (°C)	$T_{m(d)}$ (°C)	T_e (°C)	$T_{m(ice)}$ (°C)	T_h (°C)	NaCl equiv	(wt %)		
Ni-Co-As stage										
Vc-w (<15 μm) H ₂ O-CO ₂ -CH ₄ -N ₂ (<40% H ₂ O)		-23.2/11.7 (L and V) 15 L and 10 V	3.5/15.1 22	-50/-28	-10.5/-1.3 (-4) 29	284/410 V (320) 17	1 to 3		CO ₂ : 20–81 mol % CH ₄ : 12–76 mol % N ₂ : 1–25 mol % H ₂ S <0.5 mol % Graphite	
Lc (<10 μm) H ₂ O-CO ₂ -CH ₄ -N ₂ (<10% H ₂ O)		-17.5/+0.6 (L); 19 and -56.4/-40.4 (L); 8								
Lw (<15 μm) H ₂ O-CO ₂ -CH ₄ -N ₂ (>50% H ₂ O)		-4.3 to +10.3 (L and V) 5	3/13.3 6			288 to 360 L 7				
Lw-c (<10 μm) (>70% H ₂ O)			3/16.7 (15.5) 19			206/373 L (300 \pm 40) 42	(avg 6.7)			
Ag ore stages										
Lw1 (<15 μm)/QIII (80–90% H ₂ O liq)			T_{m(hh)} 11/12	-66/-44	-28.9/-12.8 (-24 and -16) 75	133/216 L (170 \pm 20) 79	16.7 to 26		Solids:illite	
Sphalerite I (Lw1 and Lw2) (<20 μ m)						117/175 L (140/180) 52			Traces of CH ₄ and N ₂	
Lw2 (<10 μm) (80–90% H ₂ O liq)				-57/-48 (-51 \pm 2)	-12.3/-1.9 (-6) 155	118/242 L (180) 150	3.2 to 13 (avg 9)		Solids:illite Traces of CH ₄ and N ₂	
Lw2b (10–30 μm) H ₂ O-N ₂ -CH ₄ -CO ₂ (80–90% H ₂ O liq)				up to -24	-9.1/-0.2 (-4 \pm 2) 168	160/220 L (180) 146	0.4 to 13 (ag 6.5)		N ₂ : 36–65 mol % CH ₄ : 8–48 mol % CO ₂ : 7–35 mol % Carbonate (c)	
Lw3/1 (<10 μm) (H ₂ O 20–90%) (studied FI 70–90% H ₂ O liq)				-55/-45	-26.6/-15.3 (-20 \pm 1) 18	118/240 L (180/200) 42	19 to 26			
Lw3/2 (<10 μm) (90–95% H ₂ O liq)					-28.2/-15.4 (-22) 26	73/111 L (80 \pm 10) 40				
Late base metal-Ag stage										
Sphalerite II (aqueous FI) (reaching 30 μ m) (90% H ₂ O liq)			T_{m(hh)} -11.5/-5.8 5	-63/-49	-23.4/-18.9 7	69/93 L or D 7	NaCl + CaCl₂ 25.8 to 26.3			

Notes: The ranges, modes in brackets, and number of measurements (in bold) are given for each microthermometric parameter; abbreviations: $T_{m(CO_2)}$ = melting temperature of volatile phase, $T_{h(CO_2)}$ = homogenization temperature of volatile phase to the liquid (L) or vapor (V), $T_{m(d)}$ = melting temperature of clathrate, T_e = eutectic temperature, $T_{m(ice)}$ = melting temperature of ice, $T_{m(hh)}$ = melting temperature of hydrohalite, T_h homogenization temperature to the liquid (L), vapor phase (V) for aqueous-carbonic fluid inclusions; all of the values are in °C

–59.1°C, $T_{h(\text{CO}_2)}$ from –4.3° to +10.3°C to the carbonic liquid or vapor phase, $T_{m(\text{cl})}$ from 3° to 13.3°C, and T_h from 288° to 360°C to the aqueous liquid phase. The volatile phase is dominated by CO_2 , followed by CH_4 , and then N_2 (Table 1).

The Lw-c FI, generally <10 μm in size, are water dominated (>70 vol % H_2O), with volatiles detected by the nucleation of clathrates during microthermometric studies and confirmed by Raman spectroscopy. The most abundant type is Lw-c, occurring as scattered fluid inclusions in Vc-w/Lc clouds or mostly secondary fluid inclusions in early quartz types (especially QI). The T_e values range between –50° and –28°C, $T_{m(\text{ice})}$ from –10.5° to –1.3°C (some values reaching –19°C), $T_{m(\text{cl})}$, when measured, range from 3° to 16.7°C, and T_h from 206° to 373°C to the aqueous liquid phase. The volatile phase analyzed by Raman spectroscopy for Lw-c FI, which nucleates clathrate, shows overall similar contents for CO_2 , CH_4 , and N_2 (Table 1). The average salinity calculated using microthermometric data ($T_{m(\text{cl})}/T_{m(\text{ice})}$) and the volatile composition (Raman spectroscopy) is around 6.7 wt % NaCl equiv.

The Lc, Vc-w, Lc-w, and Lw-c FI sometimes contain a dark solid identified as graphite by Raman spectroscopy.

Base metal stage (sphalerite I-(chalcopyrite)-galena): Fluid inclusions associated with the base metal sulfide stage (Lw1) (Table 1) are two-phase FI observed in the inner growth zones of QIII (Fig. 9a) and as primary FI in sphalerite I. Secondary Lw1 FI are found in FIP crosscutting QI and QII.

In the growth zones of QIII, primary Lw1 FI (<15 μm , 80–90 vol % liquid H_2O) have T_e values within the –65° to –60°C range, $T_{m(\text{ice})}$ range from –26.3° to –14.9°C (mode = around –25° \pm 1°C) and T_h from 133° to 192°C to the aqueous liquid phase. Fibrous crystals were observed in Lw1 FI and are identified as a K mica, likely illite by Raman spectroscopy. The Lw1 secondary FI observed in FIP crosscutting QI and QII have T_e values from –66° to –44°C, $T_{m(\text{ice})}$ from –28.9° to –12.8°C, and T_h between 134° and 216°C to the aqueous liquid phase. The salinity for Lw1 FI from the QIII base metal stage was estimated to range between 16.7 and 26 wt % NaCl equiv.

Sphalerite contains primary and secondary aqueous FI with $T_{m(\text{ice})}$ values from –24.6° to –3.2°C and T_h from 115° to 175°C to the liquid phase. The salinity of the primary Lw1 in sphalerite ranges from 22 to <26 wt % NaCl equiv.

Ag ore stage: The identification of the fluids synchronous with the main Ag deposition stage was based on the textural relationships between gangue and ore minerals. Thus, aqueous two-phase (L-V) to multiphase (L-V-solids) Lw2 primary FI (mainly < 10 μm , 80–90 vol% liquid H_2O) were found in QIV in close association with the Ag ores (Fig. 9b-d). Secondary Lw2 FI are observed as FIP in QIII, sphalerite I (Fig. 9f), and in pre-ore-stage quartz. Raman analyses suggest that the solid phases in Lw2 FI are K micas, most likely illite. No halite daughter crystals were observed. The T_e values range from –57° to –48°C. For the primary FI in QIV, $T_{m(\text{ice})}$ range from –9.1° to –1.9°C (mode at –6.0°C), and T_h from 118° to 230°C to the liquid phase (mode around 170°C). The $T_{m(\text{ice})}$ values of the secondary Lw2 FI in QIII range from –12.3° to –3.4°C (mode –5.5° to –6.0°C), and T_h from 127° to 242°C to the liquid phase (Table 1). No clathrate could be observed, but traces of gases were found using Raman spectroscopy. Unfortunately the small size of the gas bubble and its movement did

not permit quantitative measurements. The salinity of Lw2 was estimated in the H_2O -NaCl system to range from 3.2 to 16.2 wt % NaCl equiv.

Rather large fluid inclusions, the so-called Lw2b (15–20 μm , reaching 30 μm , 80–90 vol % H_2O in general), were found as primary FI in fully recrystallized microdomains from early quartz (QI) and sometimes as secondary FI (Fig. 9e). They are attributed to the Ag stages as their T_h and T_m ice values are similar to those for Lw2 FI. The T_e values range from –58° to –33°C, and $T_{m(\text{ice})}$ for most FI are from –9.1° to –0.2°C (mode at –4° \pm 2°C) corresponding to salinities of 0.4 to 13 wt % NaCl equiv. The T_h values range from 160° to 220°C to the aqueous liquid phase (Table 1) with a mode around 180°C. No clathrates were observed but traces of gases were found by Raman spectroscopy, where N_2 is dominant and accompanied by CH_4 and CO_2 (Table 1). Euhedral carbonate crystals identified by Raman spectroscopy are present in Lw2b FI.

Late brines Lw3: Dolomite III contains aqueous two-phase FI (Fig. 9g) characterized by an irregular shape. Necking down and natural decrepitation are frequently observed. Single-phase FI (liquid water) are frequent and sometimes nucleate a vapor bubble under freezing. The small size of these fluid inclusions (<10 μm) and the cloudy appearance of the host dolomite make microthermometric investigations very difficult. Only fluid inclusions with a relatively regular shape and which are apparently not affected by necking down were studied to avoid the effects of post-trapping changes.

Two types of aqueous FI (Lw3/1 and Lw3/2) were distinguished in dolomite III on the basis of their T_h value. Both Lw3/1 and Lw3/2 FI were observed in many dolomite samples with the dominance of Lw3/2 in clear dolomite and in some samples corresponding to dolomite filling flat-lying veins (low-angle dipping). The primary or secondary character of Lw3 FI cannot be established because of the FI abundance in dolomite and FIP are not easily distinguished.

The T_e values range from –55° to –45°C for Lw3. The Lw3/1 FI have $T_{m(\text{ice})}$ values between –26.6° and –15.3°C (mode = –20° \pm 1°C) and T_h range from 118° to 240°C to the liquid phase with a mode around 180° to 200°C. Lw3/2 FI have $T_{m(\text{ice})}$ values from –28.2° to –15.4°C (mode at –22°C), similar to the values from Lw3/1 but with a lower T_h that ranges from 73° to 111°C to the liquid phase (mode = 80° \pm 10°C). The salinity for the Lw3 (/1 and /2) fluid inclusions is within the 19 to 26 wt % NaCl equiv range.

Some clear crystals of sphalerite II display relatively large two-phase primary aqueous fluid inclusions (reaching a width of 30 μm) (flw = 10–15 vol %). These fluid inclusions have T_e values within the range of –63° to –49°C, $T_{m(\text{ice})}$ ranges from –23.4° to –18.9°C, $T_{m(\text{hh})}$ from –11.5° to –5.8°C, and T_h to the aqueous liquid phase from 69° to 93°C. The salinity was calculated in the H_2O -NaCl- CaCl_2 system (for FI with $T_{m(\text{ice})}$ range from –23.4° to –22.8°C and $T_{m(\text{hh})}$ from –9.5° to –5.8°C) and ranges from 20.0 to 21.3 wt % NaCl equiv and from 4.8 to 6.3 wt % CaCl_2 equiv (25.8–26.3 wt % NaCl + CaCl_2 equiv).

Ion chemistry of mineralizing fluids

LA-ICP-MS data: Representative FI related to the Ag stage (Lw1, Lw2, and Lw2b FI) were analyzed by LA-ICP-MS. Special attention was paid to the quantitative determination of Ag and the associated metal concentrations in the brines. The data

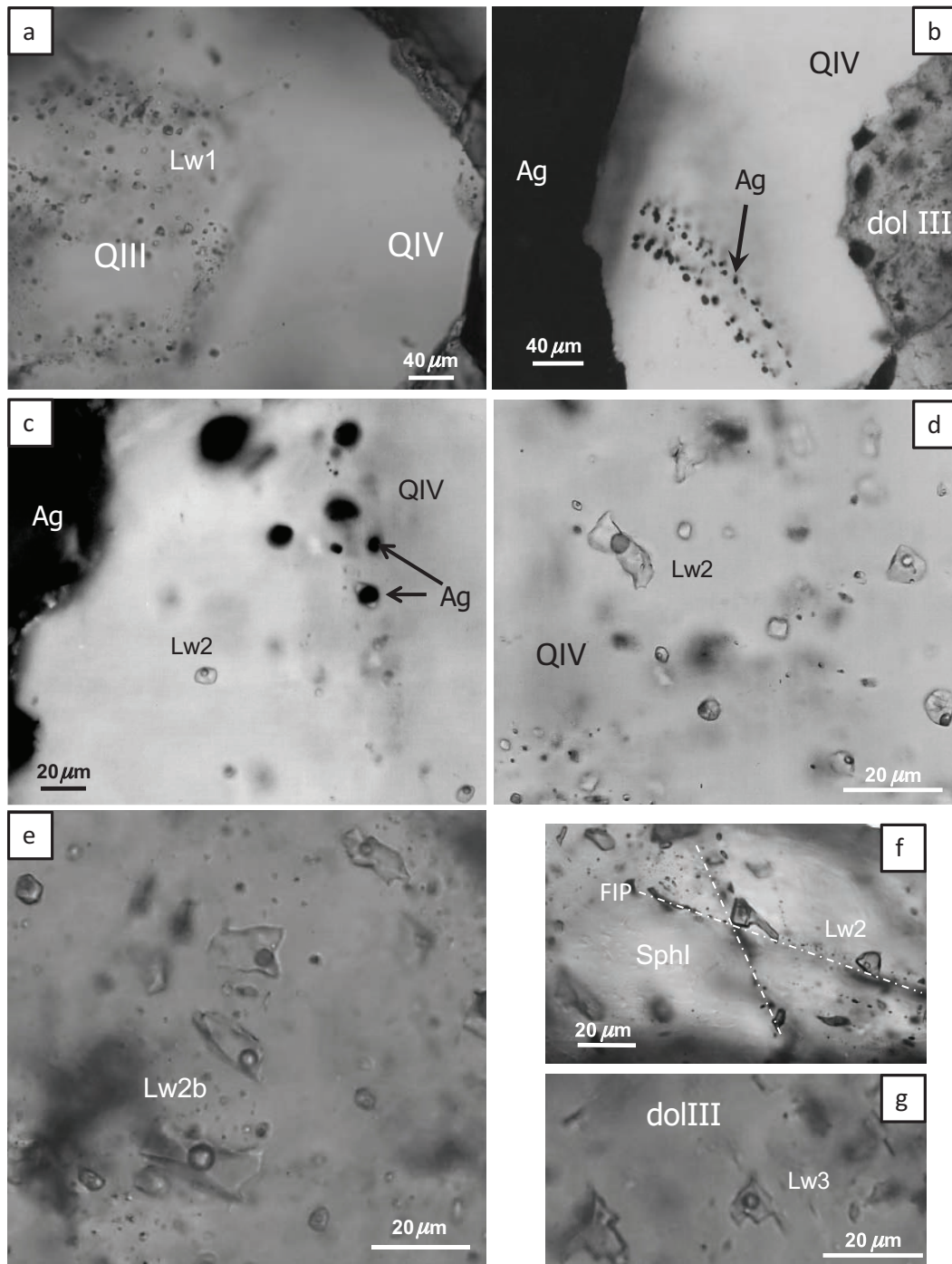


Fig. 9. Fluid inclusion types involved in the Ag deposition process. (a). QIII with abundant Lw1 fluid inclusions (brines). (b) and (c). QIV with primary and pseudosecondary Lw2 fluid inclusions and Ag solid inclusions (arrows). (d). Lw2 fluid inclusions with K micas in QIV. (e). QI recrystallized quartz and Lw2b fluid inclusions. (f). Lw2 fluid inclusions in FIP crosscutting sphalerite I (SphI). (g). Aqueous fluid inclusion Lw3 in dolomite III (dolIII). A detailed description of each fluid inclusion generation is given in the text.

are given in mmol/kg solution (Table 2; corresponding concentrations in ppm also are indicated), and plotted in binary diagrams (Fig. 10) for the different cation pairs or ratios in order to discriminate the main fluid end members (Fig. 11).

The major cations: The Lw1 and Lw2 brines in QIII and QIV, respectively, show that Na is the dominant cation in

most cases (average ranges from 2,830 mmol/kg (for Lw1) to 1,210 mmol/kg (for Lw2); 65,100–27,800 ppm, respectively). Compared with the Lw2b fluid (Fig. 11), the brines are enriched in Na and K (average K content between 1,710 mmol/kg (for Lw1) and 811 mmol/kg (for Lw2); around 66,900–31,700 ppm, respectively).

Table 2. Summary of the LA-ICP-MS Results for Fluid Inclusions Involved in Ag Deposition at the Imiter Deposit

Sample no.	Na	Mg	K	Ca	Mn	Fe	Sr	Cu	Zn	Ag	Ba	Pb	As	Sb	Na/Ca	Na/K	
<u>Lw1 fluid inclusions</u>																	
IM3-6	3,190	179	1,935	nd	nd	53	37	nd	7	14.7	7.3	3.5	na	na		1.6	
	2,659	317	1,392	296	13	51	32	nd	7.8	6.7	6.4	7.6	na	na	9	1.9	
	2,477	106	2,650	149	9	43	21	2.4	75.2	2.7	8.2	4.4	na	na	16.6	0.9	
	2,930	139	2,380	nd	nd	nd	23	nd	3.3	4	6.4	3.5	na	na		1.2	
	1,989	380	1,627	456	3	128	11	3.3	-	3.8	2.7	7.9	na	na	4.4	1.2	
IS3-1	3,243	364	1,299	nd	nd	nd	24	nd	4.5	2	10.3	3	na	na		2.5	
	3,705	290	941	nd	190	nd	110	nd	nd	29.6	32.2	10.4	na	na		3.9	
	2,709	696	958	nd	nd	nd	104	nd	nd	1.8	29.4	3.7	na	na		2.8	
IS3-2	3,788	341	674	nd	nd	67	23	-	15.2	20.8	1.4	3.1	na	na		5.6	
	2,473	406	2,135	nd	42	133	nd	nd	nd	11.8	-	7.9	na	na		1.2	
IS3-3	2,942	693	675	nd	7	89	42	2	nd	17	19.3	9.7	na	na		4.4	
	3,301	393	1,136	nd	nd	25	36	3.4	nd	5.4	18.2	1.2	na	na		2.9	
	2,613	384	2,029	nd	7	31	88	3	2.3	2.7	21.7	2.6	na	na		1.3	
Ib and Id	2,236	80	2,841	nd	3	nd	30	nd	0.6	7.4	10.3	0.3	1.5	15.3		0.8	
	1,786	170	3,157	nd	13	nd	31	nd	nd	2.8	9.7	2.8	11.2	13		0.6	
	3,239	166	1,522	226	nd	nd	nd	nd	nd	2.6	nd	nd	nd	nd	14.3	2.1	
<u>Lw1-Lw2 fluid inclusions</u>																	
Ib-Id	1,584	20	705	39	nd	nd	6	nd	nd	1	nd	nd	nd	nd	40.6	2.2	
	774	58	1,181	nd	1	nd	3	nd	2.8	0.3	0.3	1	0.8	2.5		0.7	
	1,466	94	641	nd	2	2	10	3.7	7.9	0.4	2.6	1.2	1.6	4.4		2.3	
	1,548	68	684	100	1	6	3	9.5	9.1	0.3	0.4	0.4	0.7	3.3	15.5	2.3	
	1,129	48	1,098	63	6	3	5	nd	nd	0.7	0.1	nd	nd	nd	17.9	1	
	511	95	1,712	46	7	15	5	nd	2.2	0.3	7.7	0.1	0.1	2.8	11.1	0.3	
	1,204	10	855	182	2	nd	14	nd	nd	0.2	5.3	0.1	0.2	5.5	6.6	1.4	
	1,255	17	729	81	2	nd	13	nd	nd	0.1	0.9	0.1	nd	3.7	15.5	1.7	
	1,006	273	494	nd	1	nd	3	nd	nd	0.4	nd	0.1	nd	0.1		2	
	1,138	308	550	nd	1	nd	4	nd	nd	0.5	nd	0.1	nd	0.1		2.1	
	1,726	nd	268	nd	nd	nd	12	nd	nd	0.4	2.3	1.5	2.1	nd		6.4	
	<u>Lw2b fluid inclusions</u>																
	Sample no.	Na	Mg	K	Ca	Mn	Fe	Sr	Cu	Zn	Ag	Ba	Pb	Na/Ca	Na/K		
R2	1,860	nd	nd	272	nd	nd	14	na	na	0.1	0.8	nd	6.8				
	1,525	26	93	260	nd	1	9	na	na	0.1	nd	nd	5.9	16.4			
	1,392	258	50	330	nd	3	9	na	na	0.1	1.4	nd	4.2	27.8			
	1,798	93	44	251	nd	5	8	na	na	0.1	1.8	0.3	7.2	40.9			
R2/b	892	53	103	153	3	35	21	0.3	0.6	0.3	6.8	0.4	5.8	8.7			
	862	130	151	64	1	15	20	0.1	0.5	nd	1.4	0.1	13.5	5.7			
	761	128	84	166	1	63	19	1.9	0.6	0.3	17.8	0.3	4.6	9.1			
	725	201	51	131	1	47	nd	0.4	0.4	nd	7.8	0.5	5.5	14.1			
	796	65	86	288	3	10	5	0.6	0.4	nd	0.9	0.2	2.8	9.3			
	960	183	87	66	< 1	nd	nd	nd	nd	0.3	0.5	0.5	14.6	11			
	1,030	22	147	158	1	37	10	2	0.2	0.4	1.2	0.7	6.5	7			
	1,199	17	148	63	nd	nd	5	nd	nd	nd	0.5	< 0.1	19.1	8.1			
	731	73	139	289	< 1	nd	4	nd	1	0.1	1	< 0.1	2.5	5.3			
	779	83	86	280	1	24	12	0.2	1.3	nd	30.6	0.5	2.8	9			
	899	12	64	293	6	28	nd	0.7	2.8	0.1	2.5	0.9	3.1	14.1			
985	108	58	145	nd	51	6	0.7	0.1	nd	0.4	< 0.1	6.8	17				
928	198	83	72	2	46	7	5.4	0.4	nd	0.6	0.1	13	11.1				
I12	1,242	250	74	218	1	11	1	na	na	0.2	0.4	1	5.7	16.8			
	930	152	81	40	2	11	16	0.1	0.4	0.1	2	0.2	23.2	11.4			
	917	47	171	106	nd	10	4	0.3	nd	nd	0.5	nd	8.7	5.4			

Notes: Absolute element concentrations from the LA-ICP-MS analysis are given in mmol/kg solution; abbreviations: na = not analyzed, nd = not detected

In addition, the Lw1 brine is enriched in Mg (always detected, average content of about 320 mmol/kg; 7,800 ppm), Mn (avg 32 mmol/kg; about 1,800 ppm), Sr (avg 44 mmol/kg; 3,800 ppm), and Ba (avg 13 mmol/kg, 1,800 ppm). The Mg content is variable in Lw2 and is generally <100 mmol/kg solution (<2,400 ppm) with two outliers reaching 300 mmol/kg solution. The Ca content is low and frequently close to the detection limit in most Lw1 FI, and of about 85 mmol/

kg (3,400 ppm) in Lw2 FI (Table 2). The Lw2 fluid shows relatively low average Mn, Sr, and Ba contents, around 2.6, 7.1, and 2.5 mmol/kg, respectively (140, 620, and 340 ppm, respectively), which are roughly similar to the Lw2b contents. For the Lw1 and Lw2 brines, Na is correlated with Mg and Sr and is slightly correlated with Ca and Ba but is anticorrelated with K (Fig. 10). Strontium is correlated with Ba and slightly correlated with Ca.

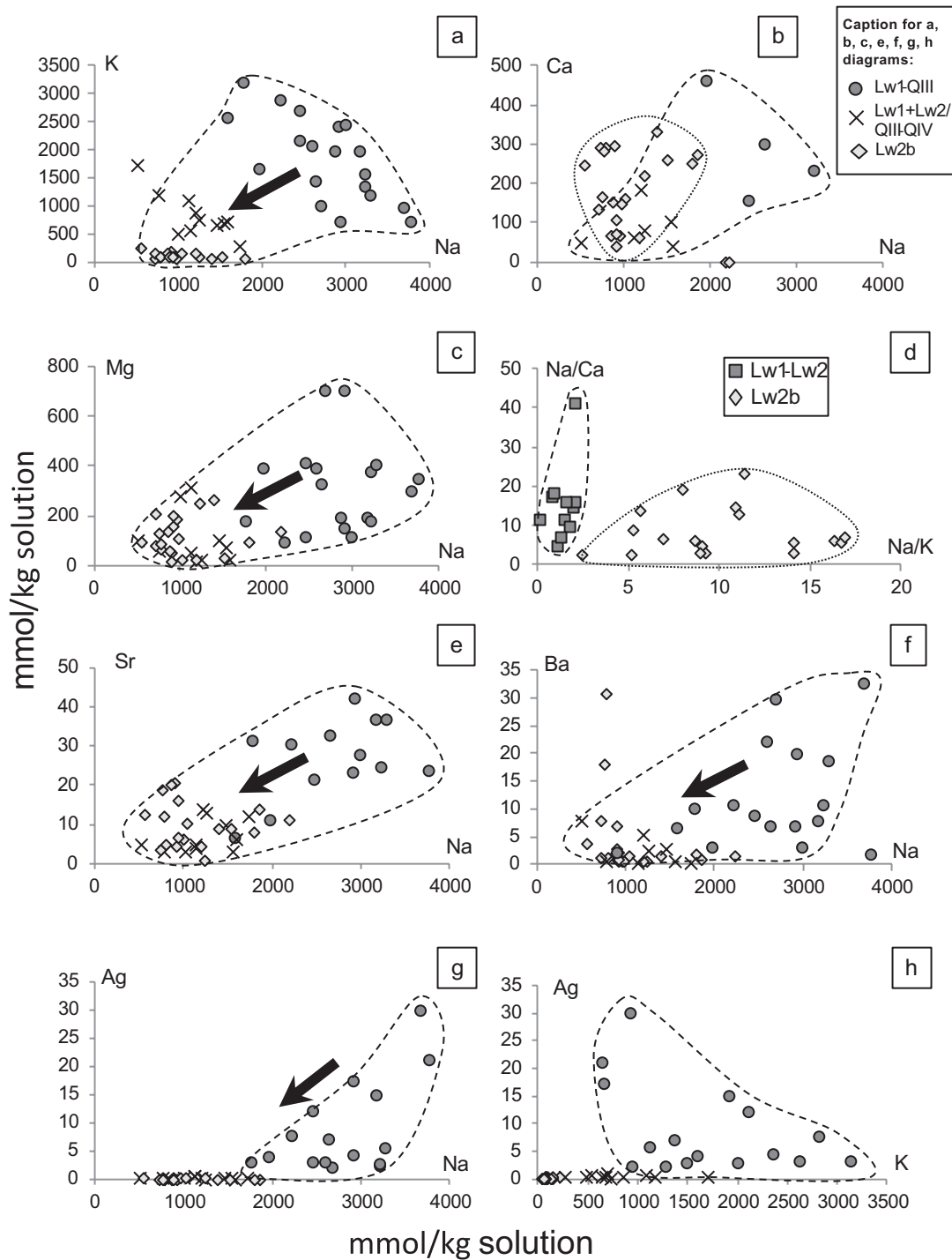


Fig. 10. (a), (b), (c), (e), (f), and (g). Na-Ca-K-Mg-Sr-Ba-Ag relationships in fluid inclusions from the Imiter deposit analyzed by LA-ICP-MS (data in mmol/kg solution). (d). Na/K vs. Na/Ca molar ratio diagram applied to LA-ICP-MS data from the two fluids involved in Ag deposition.

In the Lw2b fluid inclusions, Na is the dominant cation with an average content of 1,060 mmol/kg solution (24,400 ppm); the average Ca, Mg, and K contents are 182, 110, and 95 mmol/kg, respectively (Table 2), (7,300, 2,700, and 3,700 ppm, respectively). Magnesium is present in relatively low contents (average content around 2 mmol/kg solution, 50 ppm). The Sr content ranges from 1 to 21 mmol/kg (avg around 10 mmol/

kg, 880 ppm); Ba ranges from 0.4 to 30.6 mmol/kg (Table 2) (50–4,200 ppm). Sodium is anticorrelated with K but there is no anti- or correlation between any of the other elements (Fig. 10).

With regards to the major cations, the Na/Ca molar ratio (Na/Ca (m)) ranges from 11 to 18 for the brines and is around 8 for the Lw2b fluid. The average Na/K ratio (m) is around 2

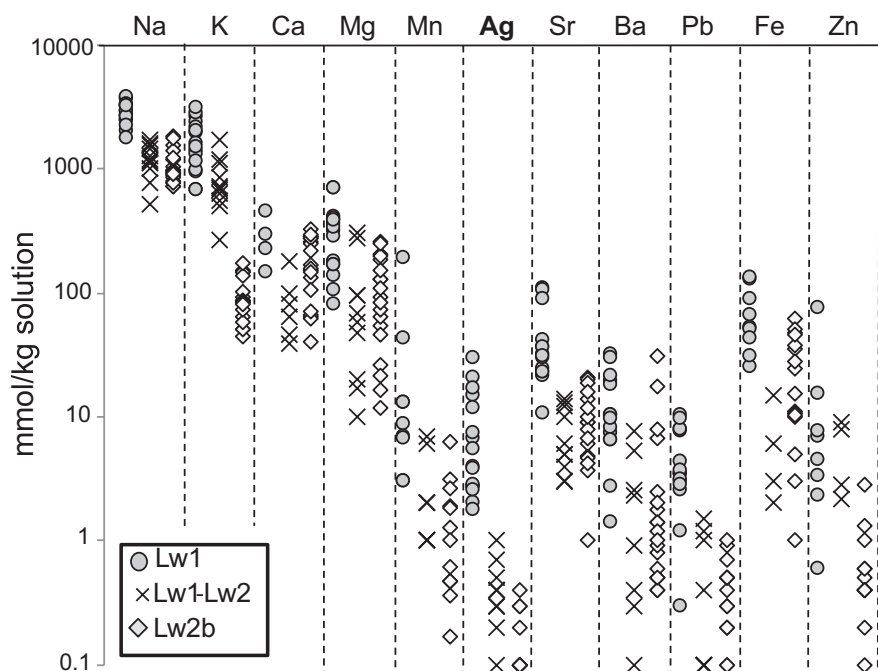


Fig. 11. Range of the major, minor, and trace element compositions (in mmol/kg of solution) of the Lw1-Lw2 (Ag brines) and Lw2b fluid inclusions from the Imiter deposit, analyzed by LA-ICP-MS.

for the Ag brines and 13 for the Lw2b fluid. The Na/Mg ratio (m) ranges from 12 for Lw1 to 36 for Lw2 FI and from 4 to 72 (avg 20) for Lw2b. Finally, the average Ca/Mg molar ratio ranges from 1.2 (for Lw1) to 4.7 (for Lw2) and is 3.8 for the Lw2b fluid.

Ag concentration in the ore fluids: The Ag concentrations were determined in Lw1 and Lw2 brines and Lw2b FI. The Lw2b FI are Ag poor and the Ag concentration ranges from below the detection limit ($5 \cdot 10^{-3}$ – $9 \cdot 10^{-3}$ mmol/kg, 0.5–1 ppm) to 0.4 mmol/kg (around 40 ppm) at the most.

The Lw1 and Lw2 (respectively from QIII and QIV) FI have an Ag concentration that ranges from 1.8 up to 29.6 mmol/kg for Lw1 (up to 3,200 ppm Ag, avg Ag around 900 ppm) and 0.1 to 1 mmol/kg for Lw2 (avg 0.4 mmol/kg, 40 ppm). Silver is correlated with Na and Sr and anticorrelated with K (Fig. 10).

The LA-ICP-MS analyses of the FI were carried out along profiles starting from the core of the QIII crystal to the later QIV crystal (Fig. 12). The Ag concentrations decrease from fluid inclusions located in the core of the QIII crystals (Lw1 FI) to the rim of the QIV crystals (Lw2 FI).

Transition metals and metalloids: The Fe content is high in the Lw1 brine (avg around 69 mmol/kg, 3,850 ppm, when detected) and is rarely detected in Lw2 (avg around 6.5 mmol/kg, 360 ppm). The Fe average content is around 25 mmol/kg solution (1,390 ppm) in the Lw2b fluid.

The Lw1 Ag-rich brine displays relatively high Pb concentrations that range from 0.3 to 10.4 mmol/kg (avg 4.8 mmol/kg, 990 ppm) compared with Lw2 (Pb content ranges from 0.1–1.2 mmol/kg and avg at 0.5 mmol/kg, around 100 ppm). When detected in the Lw2b fluid inclusions, Pb has a low content <0.1 to 1 mmol/kg (avg at 0.4 mmol/kg, 80 ppm). Copper ranges from 2 to 3.4 mmol/kg solution when detected in

Lw1 (avg 2.8 mmol/kg, 180 ppm) and is rarely detected in the Lw2 fluid (avg 6.6 mmol/kg, 420 ppm). Copper is present in most Lw2b fluid inclusions but in low concentrations (avg 1.1 mmol/kg, 70 ppm). The Zn content is low in the Lw2b fluid inclusions (avg at 0.7 mmol/kg solution, 46 ppm) compared with the Lw1 brine (avg 14.5 mmol/kg, 950 ppm) and Lw2 fluid (avg 5.5 mmol/kg, 360 ppm). Arsenic and Sb seem to be relatively enriched in Lw1 compared with the Lw2 fluid, especially Sb (avg 14.2 mmol/kg for Lw1 and 2.8 mmol/kg in Lw2, 1,730 and 340 ppm, respectively). For all of the analyzed fluid inclusions (Lw2b, Lw1, and Lw2), Co and Ni are below the detection limit (around 1 ppm).

Crush-leach data-Halogen signature: Halogens, Cl, Br, and to a lesser degree I, can be used to distinguish the source of fluids (Bohlke and Irwin, 1992) because they are conservative in solution and are relatively unaffected by fluid-rock interactions (Banks et al., 1991). At Imiter, the molar Cl/Br ratios are 330 for Ag quartz and 384 for dolomite. In the Cl/Br versus Cl diagram (molar ratios, Table 3; Fig. 13), the composition of the brines lies close to the seawater evaporation trend (Fontes and Matray, 1993).

Isotopic data

Both Ag quartz-dolomite veins and their immediate host rock (black shale rich in muscovite), as well as barren dolomite veins outside the mineralized zone (<1 km west of the Imiter mine), were analyzed for isotopic investigations: O on quartz, C and O on dolomite, H on quartz and on dolomite-hosted FI. Mineralized quartz corresponds to a mixture of QIII and QIV because it was not possible to separate the two quartz generations; however, QIII is dominant in the sample and the data can be considered as valid for characterizing the Ag brines (i.e., Lw1 fluid). Barren quartz is the recrystallized

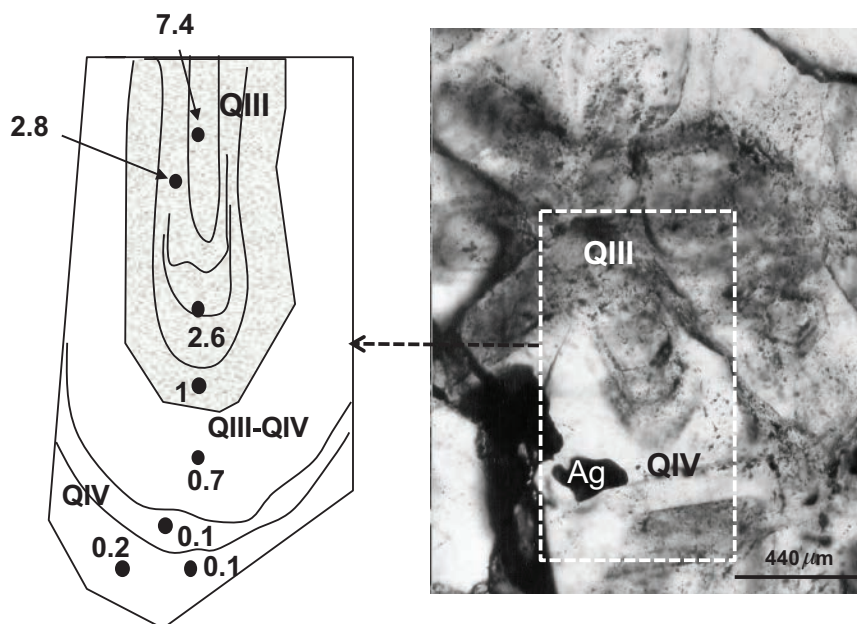


Fig. 12. Location of the LA-ICP-MS analysis on fluid inclusions in a QIII to QIV quartz area and the corresponding Ag content in mmol/kg solution.

Table 3. Halogen and Sulfate Composition of the Fluid Inclusions (in mmol/l) and Molar Ratios from the Crush-Leach Analyses for the Imiter Late Fluids, with Data from the Zgounder Deposit (*Essarraj et al., 1998) and Bou Azzer Deposit (*Essarraj et al., 2005) for Comparison

Imiter	Crush-leach analyses						Cl/Br	Cl/SO ₄	Br/Cl
Mineral	Cl	Br	SO ₄	Cl/Br	Cl/SO ₄	Br/Cl			
Dolomite III	3731	9.7	3.7	384	1015	0.0026	<u>Bou Azzer quartz*</u>		
Dolomite III	3731	9.7	4	383	930	0.0026	356	1234	0.0028
QIII + QIV	3372	10.2	9.8	329	345	0.0030	<u>Zgounder quartz**</u>		
							350	1350	0.0029

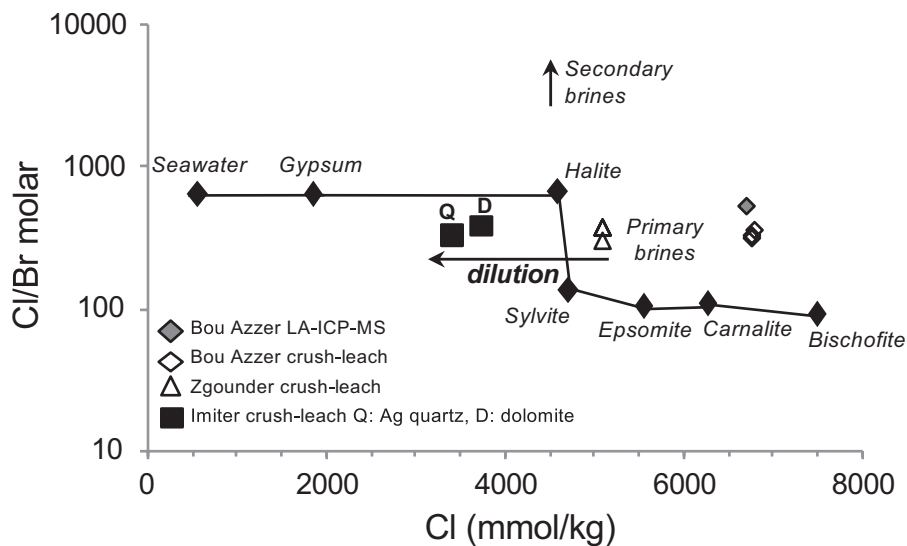


Fig. 13. Cl/Br (molar ratio) vs. Cl content of Ag fluid composition determined by crush-leach analysis from Imiter. For comparison, crush-leach analyses for Ag fluids from Zgounder (Essarraj et al., 1998) and Bou Azzer (Essarraj et al., 2005) Ag deposits and LA-ICP-MS for Ag fluid from Bou Azzer (Leisen, 2011; Leisen et al., 2013) are also plotted. Full line = seawater evaporation trend from Fontes and Matray (1993). Primary brines correspond to residual bittern brines after halite extraction; secondary brines correspond to those with salinity resulting from the dissolution of evaporitic salts.

early quartz dominated by the Lw2b fluid, and the analyzed dolomite was dolomite III.

The H, O, and C isotope composition of the veins and host rock are reported in Table 4 and are represented in Figure 14.

Stable isotope (O, C) composition of quartz, dolomite, and host rock: The $\delta^{18}\text{O}$ values range between 13.8 and 14.0‰_{V-SMOW} for Ag quartz and is 10.2‰_{V-SMOW} for the QI recrystallized quartz (with Lw2b fluid; Table 4). The $\delta^{18}\text{O}$ values of dolomite hosted by black shale coming from the central orebodies range between 22.5 and 23.4‰_{V-SMOW}, and between 23.9 and 28.9‰_{V-SMOW} in the barren area outside the mine. The majority of the $\delta^{13}\text{C}$ values of dolomite are around -10.5 ± 0.2 ‰_{V-PDB} except for one dolomite crosscutting a dolerite dike which gives a $\delta^{13}\text{C}$ value (-13.4 ‰_{V-PDB}) different from the dolomite hosted by the black shale.

Stable isotope (O, H) composition of the fluids: The δD values (± 3 ‰) are in the range of -53.8 to -65.5 ‰_{V-SMOW} for fluids from Ag quartz (QIII-QIV; Lw1/Lw2 FI) and around -28.2 ‰_{V-SMOW} for the Lw2b fluid. The δD values for the black shale range between -46 and -62 ‰_{V-SMOW}.

The $\delta^{18}\text{O}$ values of the fluids were calculated from the $\delta^{18}\text{O}$ values of the host minerals, using the fractionation factors of Zheng (1993) for H₂O quartz and those of Zheng (1999) for H₂O dolomite. The equilibrium temperature between fluid and quartz and dolomite was set to $200^\circ \pm 20^\circ\text{C}$, which was considered as a good approximation of the temperature on the basis of the average T_h of the fluid inclusions (around 180°C) and pressure corrections. The gray area in Figure 14 represents the composition of a theoretical water equilibrated with black shale at $200^\circ \pm 20^\circ\text{C}$, using the fractionation factors of Gilg and Sheppard (1995), and Sheppard and Gilg (1996).

The calculated $\delta^{18}\text{O}$ values of water (brines) in equilibrium with the quartz from the Ag stage are between 2.15 and 2.35‰_{V-SMOW}. For Lw2b, the fluid in equilibrium with the QI recrystallized quartz has a $\delta^{18}\text{O}$ value of -1.4 ‰_{V-SMOW} (Table 4). The $\delta^{18}\text{O}$ values of fluids in equilibrium with dolomite III range from 12.5 to 18.9‰_{V-SMOW}.

Data from the fluids equilibrated with the QI recrystallized quartz are close to the meteoric water composition and the seawater evaporation trend (Holser, 1979; Knauth and Beeunas, 1986; Fig. 14). Fluids from the dolomite are within the range of fluids equilibrated with the host black shale (Fig. 14). Fluids from the Ag quartz indicate an external origin as they

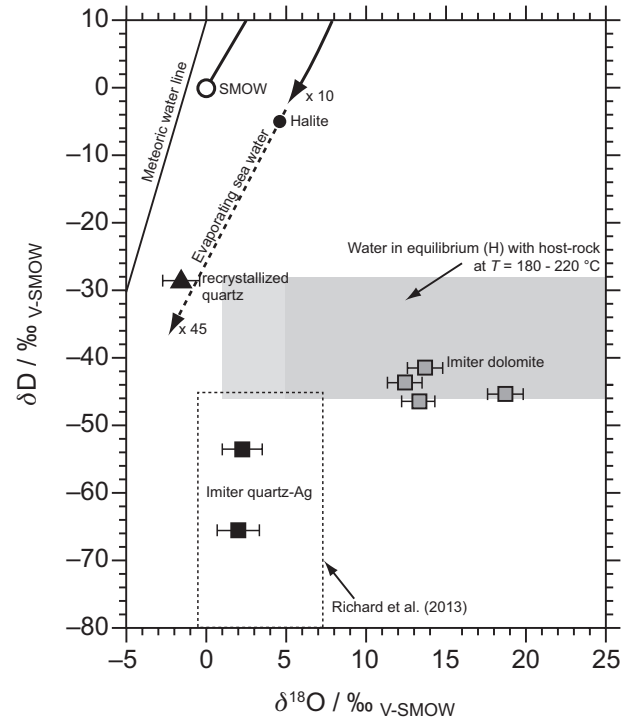


Fig. 14. Fluid stable isotope compositions ($\delta^{18}\text{O}$ and δD) from Imiter. Hydrogen isotope data of fluids from fluid inclusions and calculated oxygen data (quartz and dolomite) from measured $\delta^{18}\text{O}$, using the fractionation factors of Zheng (1993) for H₂O quartz and Zheng (1999) for H₂O dolomite. The equilibrium temperature between fluid and quartz and dolomite was set at $200^\circ \pm 20^\circ\text{C}$. The gray area in the figure represents the composition of a theoretical metamorphic water equilibrated with the black shale at $200^\circ \pm 20^\circ\text{C}$.

are not in equilibrium with the host black shale and are far from the meteoric water line (Fig. 14). The relatively low $\delta^{13}\text{C}$ values of the dolomite, close to -10 ‰_{V-PDB}, likely correspond to the contribution of an organic source of carbon present in the host black shale.

Discussion

Salinity— T_h evolution

The $T_{m(\text{ice})}$ - T_h plot (Fig. 15) shows the data obtained for the aqueous-carbonic fluids (Lw-c) from the Ni-Co-As stage and

Table 4. Stable Isotope Compositions Measured for the Host Rocks, Host Minerals, and Fluids from Imiter

Sample	Host rock		Mineralogy	Host minerals		Fluids	
	Lithology	$\delta\text{D} \pm 2$ ‰		$\delta^{18}\text{O} \pm 0.1$ ‰	$\delta^{13}\text{C} \pm 0.1$ ‰	$\delta\text{D} \pm 3$ ‰	$\delta^{18}\text{O}^a \pm 0.1$ ‰
ImA	Black shale	-52.0					
Im23	Black shale	-59.5					
Im19	Black shale	-46.7	Ag quartz	13.8		-65.5	2.2
Im54			Ag quartz	14.0		-53.8	2.4
Im12			Recrystallized QI	10.2		-28.2	-1.4
Im16			Dolomite	22.5	-10.7	-43.6	12.5
Im20			Dolomite	23.4	-10.4	-46.4	13.4
Im21			Dolomite	23.9	-13.4	-41.4	13.8
Im22			Dolomite	28.9	-10.7	-45.3	18.9

Notes: Results are given in ‰, in the δ notation relative to V-SMOW for $\delta^{18}\text{O}$ and δD and V-PDB for $\delta^{13}\text{C}$; the $\delta^{18}\text{O}$ value of the fluid is calculated from the $\delta^{18}\text{O}$ value of the host mineral following the fraction equilibrium of Zheng (1993) for quartz and Zheng (1999) for dolomite at 200°C .

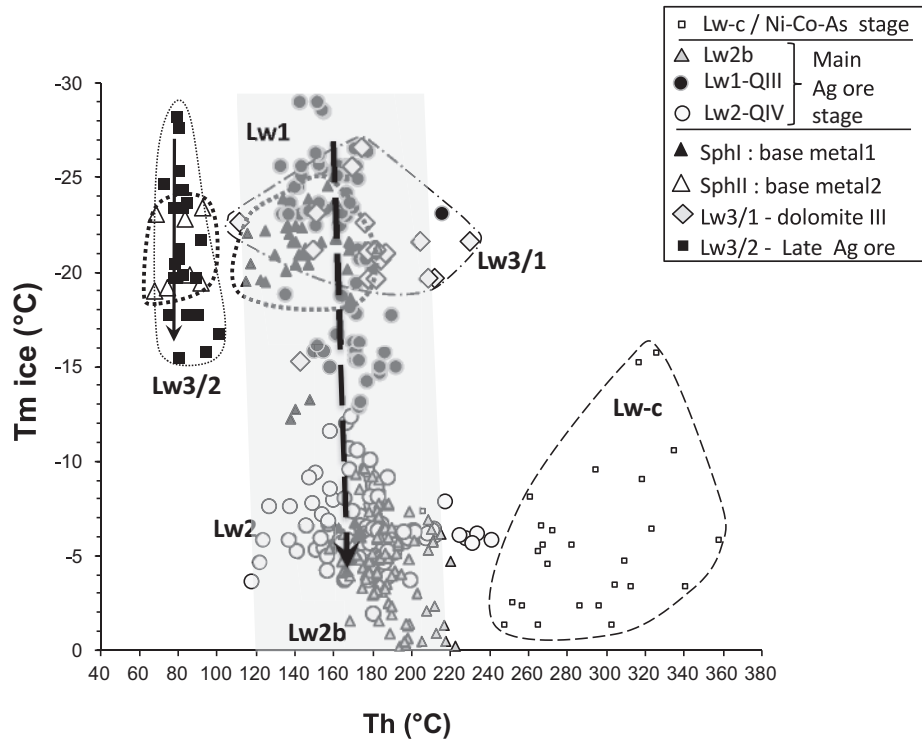


Fig. 15. $T_{m(\text{ice})}$ vs. $T_{h(L-V)}$ for aqueous and H_2O -dominated fluid inclusions from Imiter; arrows represent the trends described in the text.

the aqueous fluids (Lw1, Lw2, Lw2b, and Lw3) from the base metal and Ag stages.

The main trend for the Ag ore stage is a decrease in salinity at constant to slightly increasing T_h from the base metal brines (Lw1) associated with QIII to later low-salinity fluid synchronous with QIV and Ag deposition (Lw2 and Lw2b). The mixing trend is interpreted to relate to dilution of the brines by a low-salinity fluid.

After the main Ag stage, during or just after dolomite III deposition, the Lw3/2 brines display high salinity close to that observed for the base metal Lw1 brines, but with lower T_h values (around $80^\circ \pm 20^\circ\text{C}$). The Lw3/2 FI in dolomite III display a decreasing salinity trend at subconstant T_h (Fig. 15). These FI are considered to relate to the deposition of late Ag minerals, sphalerite II, and galena in fractures crosscutting dolomite III.

Physical and chemical conditions of the ore stages

Ni-Co-As stage: The coexistence of Vc-w, Lc-w, Lc, and Lw-c inclusions in the same fluid inclusion assemblage may suggest that, during the early quartz deposition, the earliest fluid (Lc-w likely) underwent immiscibility that resulted in the subsequent trapping of two immiscible fluids—a CO_2 -rich end member (Lc) and a water-rich end member (Lw-c). However immiscibility criteria are frequently difficult to recognize, especially for early fluids, which could be disrupted by late fluid circulations.

Using a composition-temperature chlorite geothermometer (Cathelineau, 1988), a temperature estimate within the range 240° to 340°C can be proposed for the chlorite crystallization. The chlorite crystallized after QI and slightly before

QII and the chlorite temperature domain agrees with the minimum estimates for QI at around 50 MPa also deduced from the FI T_h values (Fig. 16). The lack of biotite during the QI stage indicates a maximum temperature around 420°C (Bucher and Frey, 1994) for the QI Ni-Co-As stage and the corresponding pressure is close to 480 MPa. The immiscibility domain is probably reached in relationship with a pressure drop within the 320 to 110 MPa range, at a temperature of 350° to 400°C .

For the QII quartz and Fe-As sulfide stage, the primary Vc-w fluid inclusions show homogenization temperatures from 284°C to decrepitation temperatures around 380°C . The minimum trapping pressure is from 50 to 100 MPa and the maximum estimate is around 200 MPa, considering a maximum temperature of 420°C . Thus, the pressure decreased between the QI and QII stages and can be related either to fluid pressure fluctuations linked to the brecciation of QI or the subsequent pressure drop from lithostatic pressures toward hydrostatic pressures that are probably related to exhumation. This pressure drop is therefore probably the main driving process that controlled the immiscibility of the aqueous-carbonic fluid.

Ag ore formation at Imiter: The temperature conditions for the Ag ores were estimated considering the isochores for the Lw1 and Lw2 fluid inclusions, with minimum trapping temperatures of $200^\circ \pm 20^\circ\text{C}$ and geothermal gradients of $30^\circ \pm 5^\circ\text{C}$ (Fig. 16), a rather common value for the crust.

Chemistry and source of the Ag-brines

Two types of fluids are distinguished—a dilute Na-Ca-dominated, Ag- and metal-poor fluid represented by Lw2b

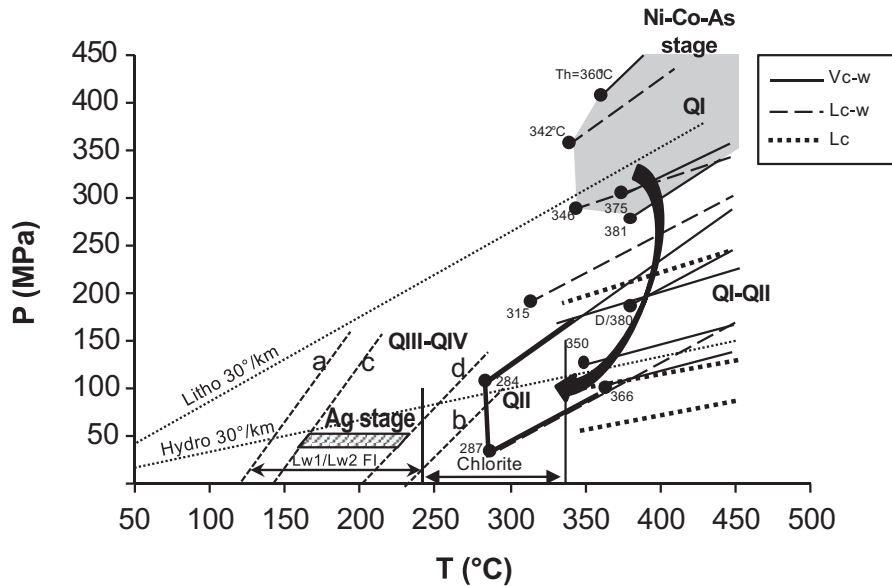


Fig. 16. P-T reconstruction diagram for the fluid circulation from preore stages and base metal/main Ag stage at Imiter (avg Lw1 and Lw2). For the fluid inclusions from early quartz QI-QII, full circles indicate the homogenization temperatures. The thermal gradient ($30^{\circ}\text{C}/\text{km}$) is drawn in thin dashed lines for the lithostatic and hydrostatic pressures. Dashed lines (a) and (b) correspond respectively to the minimum and maximum isochores, (c) and (d) correspond to the average isochore domain for the Lw1-Lw2 aqueous fluid inclusions.

inclusions, and a Na-K-Mg-(Mn)-dominated, Ag- and metal-rich brine (Lw1 fluid, metals: Pb, Zn, Fe, Sr, Sb, Table 2, Fig. 11), corresponding to the main Ag transporting fluid. The decrease of Ag concentrations in the fluids determined along the QIII growth bands toward the QIV crystals confirms that the Lw1 brine trapped in QIII represents the main Ag-bearing fluid. This brine underwent dilution during the coprecipitation of Ag and QIV, attested by the correlation between the Na and Ag contents in the brines (Fig. 10). This is probably linked to a dual process—the mixing of brines with low Ag waters, and the Ag ore deposition itself. Simultaneously to the Ag decrease from QIII to QIV, the metal decrease (mainly Mn, Sr, Ba, Pb, Fe, and Zn) from the Lw1 brine to the Lw2 fluid highlights the brine dilution by a metal-poor fluid (i.e., Lw2b fluid). Indeed, the Lw2 fluid inclusions show intermediate metal compositions between Lw2b and Lw1 (i.e., the two mixing end members, Fig. 11). The Na and K concentrations among the Lw1 and Lw2 fluids distributed along the dilution trends, which are similar to those of other cations such as Mg, Sr, and Ba. In addition, a Na-K trend along a 1/1 slope characterizes the Lw1 brines (Fig. 10) but the Na/K ratio remains very low in the 1 to 6 range.

The geochemical features of the Imiter Ag brines are similar to those of deep basinal brines (Kendrick et al., 2002; Hammerli et al., 2013). The Cl/Br molar ratios (330 for Ag quartz, 384 for dolomite) are interpreted as typical of residual bittern brines after halite extraction (Holser, 1979; McCaffrey et al., 1987; Hammerli et al., 2014) that was diluted later. The high Na/Ca molar ratios (QIII and QIV brines) as well as the high K and Ba-Sr concentrations further support the presence of bittern brines, which could have reached sylvite and epsomite saturation (Fontes and Matray, 1993). The very high K concentrations are in agreement with the precipitation of adularia, which requires a high K^+/H^+ ratio. Consequently, the

Ag brines from Imiter do not result from dissolution of salts from the Adoudounian evaporites (Infra-Cambrian) sometimes recognized as very thin layers in the eastern Anti-Atlas. The Cl/Br ratio of the Imiter brines is similar to those found in the Zgounder Ag deposit (Essarraj et al., 1998) and Bou Azzer Co-Ni-Ag deposit (Essarraj et al., 2005; Leisen et al., 2013), which are located approximately 220 and 150 km southwest from Imiter, respectively (Fig. 1).

Considering a thermal gradient of $30^{\circ} \pm 5^{\circ}\text{C}/\text{km}$, the brine temperatures of $200^{\circ} \pm 20^{\circ}\text{C}$ could correspond to maximum depths of 5 to 6 km. However, the distance to the unconformity at the age of the ore formation is unknown, and it cannot be precluded that the brines were not in thermal disequilibrium with the host rocks, as is the case in several Pb-Zn deposits. Therefore, the depth and pressure of the ore formation are rather difficult to estimate, and 50 to 60 MPa, 180° to 220°C represents the maximum likely pressure and temperature conditions.

During the Permian-Triassic, large basins formed north of the Anti-Atlas in relationship with the Atlantic opening and subsequent Atlantic rifting. For Frizon de Lamotte et al. (2008, 2009), the Anti-Atlas corresponds to an emerged area which borders a major Tethyan basin to the south with thick red beds capped by basaltic flows. Soulaïmani et al. (2014) proposed that, during the Triassic-Early Jurassic rifting, the Anti-Atlas area belonged to the uplifted shoulder of the rift zone, which extended into the Atlantic margin and High Atlas basin. The shoulder erosion sourced the red beds of the High Atlas in the north.

The Triassic clastic series to the north of the Anti-Atlas could be equivalent to the Argana Permian-Triassic series in the Atlantic domain, the thickness of which may reach 6 km. They are marked in the basement and in the Triassic and Liassic series by a thermal episode, which could have reached

185° to 210°C during 10 to 15 Ma (Huon et al., 1993), recognized in the Atlasic basins, and representing a synrift metamorphism. The “Atlasic rift” is considered to have opened at the same period. It is characterized by extensional tectonics, with the formation of sedimentary basins, the reactivation of basement faults (Laville and Piqué, 1991; Piqué and Laville, 1993, 1996), and thus during the Liassic, by the deposition of marine sequences which induced a postrift thermal subsidence stage. The latest metamorphic event, likely accompanied by hydrothermal activity (Raïs, 1992), is Triassic and is no later than early Liassic. Piqué et al. (1987) proposed that there are several lineaments in Morocco (including the Anti-Atlas) representing permanent zones of weakness that have been active from the Precambrian to the present. These structures were inherited from Precambrian orogenies and were reactivated repeatedly in the epicratonic margin (e.g., West African craton margin in the Anti-Atlas) during the Atlasic orogenies. In the eastern Anti-Atlas, former normal and inverted faults were reactivated during the Atlantic opening event (Robert-Charrue and Burkhard, 2008), leading to the formation of steep normal faults and to the intrusion of dolerite dikes and sills from the Triassic-Liassic period within the Paleozoic cover series. On this basis, Robert-Charrue and Burkhard (2008) proposed that the Triassic likely covered the Anti-Atlas, and Sebäi et al. (1991) demonstrated that in the Anti-Atlas, dolerite dikes (Fig. 17) and sills, dated between 206 and 195 Ma, are related to this rifting episode, which is synchronous with the Central Atlantic magmatic province (CAMP) activity (Verati et al., 2007). In the central Anti-Atlas, the Triassic is incompletely observed in the core of diapiric structures (Ettaki et al., 2007; Michard et al., 2008) but there is no evidence that the Triassic

series was deposited in the Anti-Atlas. If the Triassic formations did not cover the Anti-Atlas, the long-range migration of the brines expelled from the Atlasic Triassic basins may be possible for Imiter because the evaporite series are not necessarily located close to the deposit but can be laterally distant, as observed in numerous cases (for instance at Poitou High, northwestern French Massif Central, where evaporite layers are located more than 100 km from the Pb-F-Ba-related occurrences, Boiron et al., 2002, 2010). The closest known occurrence of Triassic (Norian-Rhaetian) evaporites is around 30 km north of the Imiter area (Fig. 17; El Arabi, 2007). During the Early-Middle Liassic, the Imiter area was at a distance <10 km from the deep zone of the Atlasic basin to the north (distance estimated based on data from Poisson et al., 1998).

The isotope patterns of the brines are distributed in a δD - $\delta^{18}O$ diagram along a mixing trend between evaporitic brines and low δD sedimentary fluids. Brines from Ag quartz show a ^{18}O enrichment away from the isotopic composition of meteoric water or evaporated seawater. Their ^{18}O enrichment could result from a large isotopic exchange with the host rocks including basement formations, indicating a distant source of this fluid, without equilibration with the host black shale. The ^{18}O enrichment of the Ag brines could also result from a contamination with magmatic waters resulting from volcanic activity synchronous with the opening and filling of the sedimentary basins. Despite the contamination possibilities, the brines are interpreted to be of sedimentary origin, based on their halogen signatures, that are relatively unaffected by fluid-rock interactions (Banks et al., 1991). The depletion in δD could be attributed to CH_4 oxidation (Tarantola et al., 2007). However, there is no time or genetic link between

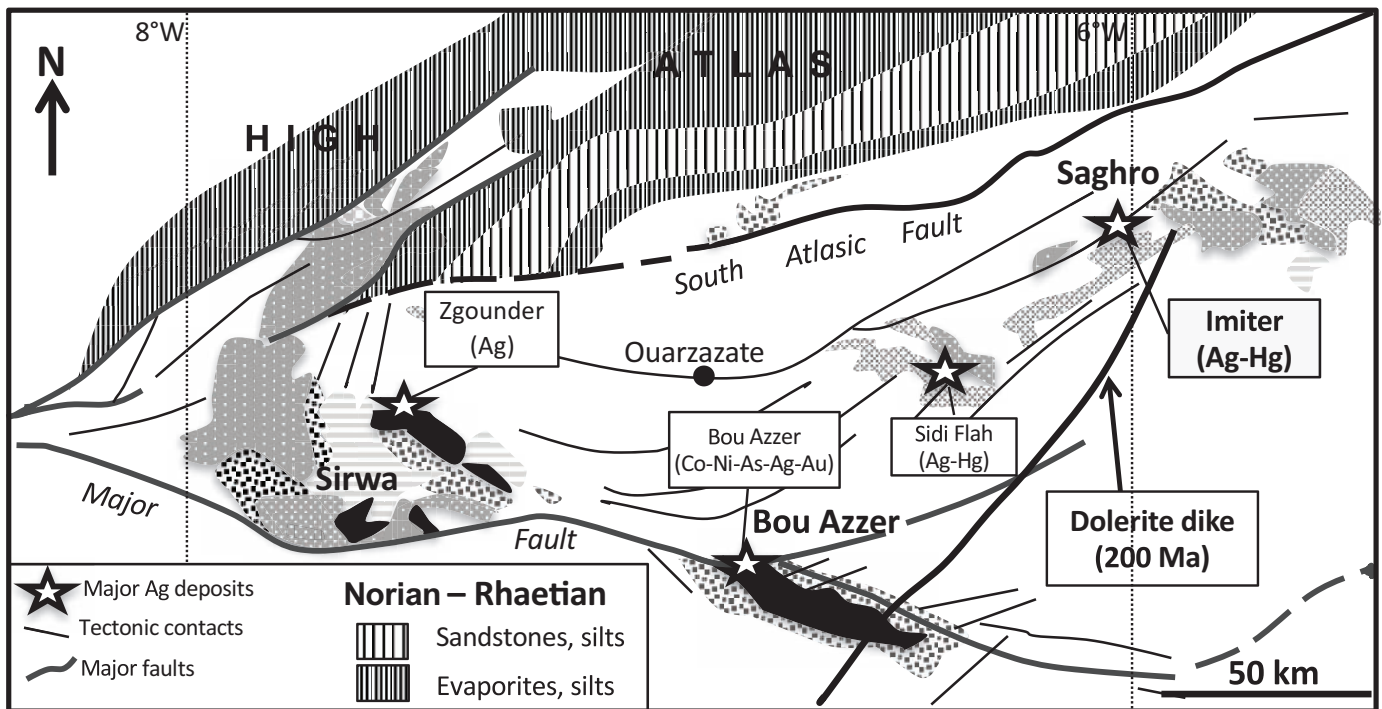


Fig. 17. The Norian-Rhaetian paleogeography north of the Anti-Atlas (north of the Imiter area), after El Arabi (2007, in Frizon de La Motte et al., 2009); see Figure 1 for the caption of the Pan-African formations.

this brine episode and any other methane-rich fluid inclusion stage. There are strong similarities between the Imiter Ag brines and evaporitic brines found in the Paleoproterozoic basin from Athabasca (Canada; Richard et al., 2013). The isotopic data of the metal-poor fluid from the QI recrystallized quartz plot close to the seawater evaporation trajectory. However, especially because of its low salinity, this fluid is interpreted as a recharge fluid of meteoric origin, in the absence of data on halogen signatures which could give more information about the fluid source.

The He isotope ratios ($R = {}^3\text{He}/{}^4\text{He}$) obtained by Levresse et al. (2004) for the Ag ore stages (quartz, dolomite, and sulfides: $R/R_a = 0.8\text{--}1.8$, R_a is the atmospheric ${}^3\text{He}/{}^4\text{He}$) are by far closer to crustal fluids ($R/R_a = <0.01$; Ozima and Podosek, 2002) and atmospheric fluids ($R/R_a = 1$) than to mantle fluids ($R/R_a = 6\text{--}9$ or above, Gautheron and Moreira, 2002; Graham, 2002), more likely indicating that the mantle contribution is negligible with regards to the Ag fluid source at Imiter. In addition, as several microsyenite and dolerite dikes are considered as synchronous to the Ag deposition (Borisenko et al., 2013), an upward deep-seated He and its mixing with the brines at that stage cannot be ruled out.

Age of the deposit

If the brines are linked to the Permian-Triassic formation, this process is younger than 260 to 200 Ma. Recently, an age of 254.7 ± 3.2 Ma was obtained by Borisenko et al. (2014), using Ar/Ar dating on adularia from the Imiter Ag ores. Adularia can therefore be attributed to a diagenetic feldspatization at an age close to the Permian-Triassic boundary, and the Ag ores that were deposited slightly later than the adularia crystallization are thus younger than 254 Ma at least.

Considering that the ore deposition at Imiter corresponds to early episodes of Triassic evaporite formation, it may be synchronous with the major stage of thermal and fluid flow in this region during the post-Proterozoic, which is attributed to the ascension of the upper mantle (Frizon de Lamotte et al., 2009) within a thin continental crust during the earliest stages of the Atlantic rifting. The ages for the African Central Atlantic magmatic province magmatism range from 202.5 ± 3.0 to 190.5 ± 1.2 Ma (Nomade et al., 2007) and this magmatic activity is confirmed by the dating of high K microsyenite dikes from the Bou Azzer deposit at 199.5 ± 2.4 and 204.5 ± 2.5 Ma (Ar-Ar data on biotite and K-feldspars, Lebedev, 1998 in Borisenko et al., 2013).

Similarities in brine chemistry, trapping conditions, and the nature of the mineral association in the three Ag deposits from the Anti-Atlas (Zgounder, Bou Azzer, and Imiter located over an area of more than 220 km in length) may suggest that a major regional stage of brine and metal migration occurred in the Anti-Atlas (Essarraj et al., 2005). A Norian age was already proposed for the Ag ores at Bou Azzer (Essarraj et al., 2005) based on adularia dating (218 ± 8 Ma, ${}^{40}\text{Ar}/{}^{39}\text{Ar}$, Levresse et al., 2001).

From a structural point of view, the first and major Ag stage may be related to the west-northwest-east-southeast shortening and corresponding dextral transpressive event described by Tuduri et al. (2005). The north-south shortening direction is controlled by a normal left-lateral motion and is considered as synchronous to the barren pink dolomite (Tuduri et al.,

2005), corresponding to the major dolomite stage (dolomite III) described in the present work.

Source of metals

Previous works on the Imiter deposit (Leistel and Qadrouci, 1991; Pasava, 1994; Baroudi et al., 1999) suggest the host black shales as a source for Ag. According to Huyck (1991), metalliferous black shales are enriched in any metal by a factor of two relative to the SDO-1 (Devonian Ohio Shale, Huyck, 1991). The Ag, Pb, Zn, As, and Ba contents are anomalously high in the Imiter host black shale (3.4, 583, 370, 170, and 1,044 ppm respectively, Pasava, 1994) compared with the SDO-1 metal contents (Ag = 0.09–0.017, Pb = 27.9, Zn = 64, As = 68.5, and Ba = 397 ppm). However, no enrichment in Cu and Hg was recorded in the Imiter black shale compared with the SDO-1 (Baroudi et al., 1999), and thus Hg was able to be scavenged from the rocks during brine migration from the Atlasic basins.

Several studies have established that likely metal sources for Pb-Zn in base metal deposits include (1) sedimentary basins (Leach et al., 2005), (2) crystalline basements (Russell, 1978; Oliver et al., 2006), and (3) the leaching of metals by fluid flow during regional metamorphism (Lebedev and Nagaytsev, 1980; Haack et al., 1984; Hammerli et al., 2015). For Imiter, ${}^{187}\text{Os}/{}^{188}\text{Os}$ values lower than 0.2 are considered by Levresse et al. (2004) as representative of a mantle source. The deep downward circulation of basinal brines into the basement rocks may be a mechanism for extraction of base metals (Russell, 1978; Boiron et al., 2010), especially at the top of the basement which generally underwent weathering before the deposition of sedimentary formations. Thus, the regolith developed during the Triassic, especially on the lithologies that are relatively enriched in Ag and Hg, such as the basic series (andesitic series and dolerite-andesite dikes at Imiter, basic dikes, ultrabasic rocks known elsewhere such as in other inliers from the Anti-Atlas) can be considered as an excellent source as the metals are liberated from their source during weathering (Boiron et al., 2010). Therefore, there is no contradiction with the extraction of metals from some of the mantle formations proposed by Levresse et al. (2004), as mafic/ultramafic units are known at the scale of the Anti-Atlas inliers, and brine circulations are inferred to have taken place over large distances.

Ore fluids and silver deposition

Silver deposition was favored in high-permeability extensional zones that were filled by quartz and Ag, followed by dolomite-galena-Ag. QIV hosts Ag microinclusions close to the Lw2 FI, and sometimes Ag particles are found inside the Lw2 FI (Fig. 9c). As established by Wilkinson (2001a), the best evidence for temporal genetic relationships between ore and gangue minerals is the occurrence of fine-grained ore mineral inclusions within the gangue mineral itself, or if the fluid inclusions contain daughter ore minerals. Thus, the trapping of Lw2 FI is interpreted as synchronous to the major Ag deposition stage.

Two contrasted fluid end members were determined by microthermometry combined with the LA-ICP-MS technique:

1. Na-K-Mg-dominated, Ag- and metal-rich brine (mainly Pb, Zn, Fe, Sr, Sb) (the Ag content reaches 29.6 mmol/kg, avg 8.5 mmol/kg). This Ag brine is synchronous with QIII

and evolved to a diluted and metal-poor fluid (especially Ag-poor, avg content = 0.4 mmol/kg) synchronous with QIV and Ag precipitation.

2. Low-salinity Na-Ca-dominated, Ag- and metal-poor fluid (avg Ag content of 0.2 mmol/kg). The dilution of the brine is probably anisothermal as a significant difference in T_h , around 40°C, characterizes the two end members. The mixing of the brines with a slightly hotter fluid end member is recorded in most F-Ba (Pb-Zn) or U deposits linked to unconformities (Boiron et al., 2010). The latter is interpreted to result from the deep convection of the recharge fluids, which then ascend along faults and are in thermal disequilibrium with the host rocks because they are heated at greater depths.

Silver is thought to have been transported in brines, likely dominantly as chloride complexes according to the thermodynamic modeling of Ag speciation in these brines (Borisenko et al., 2014; Benchekroum and Essarraj, 2015, based on data from Stefánsson and Seward, 2003; Pavlova et al., 2004, Pal'yanova, 2008). According to Pal'yanova (2008), experimental data show that the maximum silver concentrations can reach 10⁴ ppm at 500°C (under salinities from 1–5 M NaCl, and various pH and Eh conditions) and the minimum solubility is 1 ppb at 200°C (for very low salinity fluids—<1 M NaCl) regardless of the ligand considered. At Imiter, the Ag concentration in the brine is up to 30 mmol/kg (3,200 ppm, avg 900 ppm) and agrees with the experimental data from Pal'yanova (2008). The decrease in chlorinity due to dilution results in the destabilization of the Ag chloride complexes and subsequent Ag deposition (the Ag and Na contents are correlated in the brines), as suggested for numerous other Ag deposits (Beaverdall deposit in British Columbia, Godwin et al., 1986; Cobalt, Ontario, Marshall et al., 1993; and from the Anti-Atlas in Morocco—Zgounder Ag deposit, Essarraj et al., 1998, and the Bou Azzer Co-Ni-Ag deposit, Essarraj et al., 2005, among others). Mixing processes were also proposed for the Pb-Zn-(Ag) deposits in the Irish Midlands (Wilkinson, 2010b), the Alaskan Brooke Range (Leach et al., 2004), the French Pb-F-Ba deposits from the Massif Central (Boiron et al., 2002), and Upper Silesia (Poland) (Heijlen et al., 2003), among others. The hypothesis of Ag transport as sulfide complexes proposed by Levresse et al. (2004) for the Imiter deposit was based on the assumption that the ore fluids were of low to moderate salinity (0–10 wt % NaCl equiv). Our data have shown that the Ag-bearing fluid is a high-salinity brine (16.7–26 wt % NaCl equiv).

The brines related to the deposition of dolomite III, i.e., the main dolomite stage, are of a sedimentary origin. A later Ag stage seems to have occurred under lower temperature (likely <100°C) and, according to the thermodynamic data from Borisenko et al. (2014), under more acidic conditions than the first and major Ag stage. At these temperatures (and 5 M chloride solution, pH = 3.5), the Ag concentrations (dominantly as chloride complexes) are up to two orders of magnitude lower than at 200°C (Pavlova et al., 2006). This Ag stage probably corresponds to a second pulse of sedimentary brine. There is no evidence of metal remobilization from the first Ag ores at that stage.

Experimental studies on the solubility of the Zn and Pb minerals demonstrate that the Zn and Pb contents in saline

solutions strongly correlate with the temperature and salinity of the fluid (Barrett and Anderson, 1982, 1988, Crerar et al., 1985, Hemley et al., 1992, Yardley, 2005). Consequently, a dilution process is probably responsible for the deposition of sphalerite and then of galena from metal-rich brines at Imiter simultaneously with Ag precipitation.

Redox and fluid-rock interactions

According to Pasava (1994) and Baroudi et al. (1999), black shale could represent a reduced environment leading to the deposition of Ag ores at Imiter as the f_{O_2} decreases. On the basis of thermodynamic considerations, Borisenko et al. (2014) proposed that local reducing conditions together with a pH increase could produce massive Ag-Hg deposition at Imiter. The interaction between brine and black shale could have enhanced Ag deposition in addition to the effects of fluid mixing. The presence of abundant adularia crystals deposited at the QIII selvages could be related to the K-rich brines (i.e., high K⁺/H⁺ ratios). This type of adularia formation was also observed at Bou Azzer where it is inferred to be related to Ag deposition (Essarraj et al., 2005).

Proposed metallogenic model

The downward penetration of brines below the unconformity is a common process described elsewhere at the unconformity between the basement and overlying sedimentary basins in a variety of geologic contexts—Proterozoic basins (Oklo and Franceville (Gabon): Mathieu et al. (2000), Moubiya Mouele et al. (2014); Saskatchewan (Canada): Kyser et al. (2000); the Northern Territory (Australia): Derome et al. (2003); Mesozoic basins (western Europe: Boiron et al. (2002); intracontinental rifts with Mesozoic to Cenozoic sediments such as the Rhine graben (Pauwells et al., 1993; Cathelineau and Boiron, 2010) or the Southeast basin in France (Aquilina et al., 2011). In all of these examples, brine migration occurred significantly later than sedimentation. The penetration of basal fluids within the basement has also been discussed by Yardley et al. (2000), Cathles and Adams (2005), and described in southern Norway (Munz et al., 1995; Gleeson et al., 2003; Oliver et al., 2006), in Spain (Piqué et al., 2008), in various places in Europe (Muechez et al., 2005; Bouch et al., 2006), and in numerous metal deposits all around the world (Boiron et al., 2010). As shown by Boiron et al. (2010), fluid circulation at the basement/cover unconformities is of major importance for metal transfer, and fluid mixing is one of the key factors for ore formation, especially the formation of Pb-Zn, F, Ba, and U deposits from various ages. Fluid circulation is related to extensional tectonics and continental rifting. Several similarities are observed between all of these fluid systems (Boiron et al., 2010) and the Imiter fluid circulation features: (1) a wide range of fluid salinity, indicating the lack of homogeneity in the fluid chemistry at the scale of the reservoirs; (2) the deep penetration of brines through faults within the basement below the unconformity between the Precambrian-lower Paleozoic and more recent formations through major crustal faults such as the Imiter fault zone; (3) fluid movements facilitated by a discontinuous opening related to late tectonic activity linked to major geodynamic events such as the Atlantic rifting and the subsequent Central Atlantic magmatic province activity and

abnormal heat flows; and (4) fluid mixing as a major driving mechanism for metal deposition.

Our model is at variance with the magmatic models already published for Imiter (Levresse, 2001, Cheilletz et al., 2002, Levresse et al., 2004). The magmatic-related mineralization model at Imiter may be valid for the first Ni-Co-As stage, but not for the main Ag stages. Thus, magmatic fluid systems were active at the end of the Pan-African orogeny, in particular during the emplacement of the granodiorite pluton (572 ± 5 Ma, U/Pb on zircon, Levresse, 2001) and the rhyolitic intrusions (550 ± 3 Ma, Cheilletz et al., 2002). These intrusions yield to the circulation of fluid dominated by metamorphic $\text{H}_2\text{O}-\text{CO}_2-\text{CH}_4$ fluid components equilibrated with the black shales, and magmatic fluid components. These fluids are at the origin of the Ni-Co-As ores, and the crystallization of quartz Q1 and muscovite, which is dated at 563 to 577 Ma and reset to 542 to 552 Ma by the rhyolite intrusion (Ar-Ar on muscovite, Cheilletz et al., 2002).

The Ag stage is well constrained, as discussed above, by the age at 254 Ma for adularia, which precedes the main Ag stage. At these times, thermal and tectonic activities were synchronous with the first rifting episodes of the Atlantic Ocean opening. Sedimentary evaporitic series deposited in Atlasic basins subsequent to Atlantic opening and surrounding areas are the main potential source of brines likely mobilized during this major extensional tectonics. The Imiter Ag deposit follows part of the criteria defined for the MVT deposits (Leach et al., 1995). Indeed, the Ag districts represent a metallogenic province where Ag is present in most inliers in the central Anti-Atlas. In addition, Ag deposits are located around a zone of upward fluid migration (i.e., Atlasic basins) of dense basinal brines with more than 10 wt % salts. The ore deposition temperatures are low ($80^\circ\text{--}200^\circ\text{C}$) at Imiter and yielded to dolomite and feldspar crystallization.

Finally, in several MVT or basin-hosted deposits such as those from Central Tennessee and Tri-State (United States; Deloule et al., 1986), as well as Silesia (Poland) (Heijlen et al., 2003), the $\delta^{34}\text{S}$ values are around -5 to -10‰ CDT. For the Imiter Ag stage, most of the $\delta^{34}\text{S}$ values obtained by Levresse et al. (2004) range from -19 to -4‰ CDT with a mode around -9‰ CDT. These values were interpreted by Levresse et al. (2004) as having shifted toward light values by increasing contamination due to interactions with black shales. These values may in any case correspond to those from thermochemical sulfate reduction processes affecting marine-derived waters, as shown by Wilkinson (2014).

Conclusions

A revision of the paragenetic sequence and related fluid types, combined with detailed geochemical data for the Ag ore fluids allows us to revisit prior metallogenic models for Imiter and to propose a new model that reconciles the different data. A precise identification of the relative timing/textural relationships between mineralizing fluids, ore, and gangue minerals was used to determine the following:

1. The origin of the ore fluids, by combining stable isotope data, halogen signatures, and major cation chemistry, i.e., Na-K-Mg bittern brines. The low Cl/Br ratio of the Ag brines, linked to a relative Br enrichment, is typical of

residual brines after halite extraction and is similar to those of the MVT deposits. Ionic molar ratios indicate that the compositions of the Ag-mineralizing fluid from Imiter are characteristic of evaporated seawater and that the source of the salt is residual brines like those recognized in most modern sedimentary basins.

2. Bracket the range of Ag concentrations in ore fluids; this dataset is the first set of metal concentrations available for Imiter ore fluids.
3. Identify the main process driving the Ag deposition, i.e., a mixing of bittern fluids with dilute recharge fluids, which subsequently results in a decrease in the metal concentration in fluids, a process that has already been described in other base metal and major Ag deposits.
4. Relate the ore brines to extensional tectonics during the Triassic, when Atlasic basins produced hot basinal brines resulting from evaporatively concentrated seawater, comparable to MVT deposits. Sedimentary brines were likely put in motion in relationship with tectonic and abnormal heat flows linked to the significant volcanic activity synchronous with sediment deposition in Triassic basins.

This model is at variance with previous epithermal models linked to magmatic systems (Levresse, 2001, Cheilletz et al., 2002, Levresse et al., 2004 for Imiter, Leblanc and Lbouabi, 1988 for Bou Azzar). The magmatic-hydrothermal model is only applicable to the very first aqueous-carbonic fluid circulation stage at the origin of the Ni-Co-As-quartz-muscovite assemblage, and is considered as late Pan-African in age (570–550 Ma). The superposition of a new ore deposit at less than 300 Ma afterward indicates that the Imiter fault is a major lineament that was reactivated during major geodynamic events affecting the Anti-Atlas. Silver deposition has no genetic relationship with these early Pan-African events, but follows the major processes of extraction and deposition of metals by sedimentary brines, already considered as the origin of the other Ag deposits in the Anti-Atlas, and related to much later stages in the opening of the Atlantic Ocean. These events favor the penetration of recharge waters in the basement as well as bittern waters uptaking metals in the basement, likely the regolith, thanks to localized thermal anomalies exemplified by the intrusion of basic dikes and reactivation of major lineaments.

Acknowledgments

The authors would like to thank E.B. Barodi (BRPM) for authorizing a first sampling of the Imiter deposit, A. Gmira and R. Larhouti (SMI Company-MANAGEM group) for recently authorizing complementary sampling and the geologic staff of SMI Company, especially A. Gaouzi, for precious help during sampling, discussions, and logistic help at the site of the mine, and H. Aboud. D. Banks is thanked for supplying the three crush-leach analytical data. Special thanks are expressed to J. Dubessy for a discussion on the fluid composition. Sara Mullin is warmly thanked for her careful English editing of the manuscript. The manuscript benefits from the comments of D. Banks and J. Hammerli as reviewers, B. Rusk, associated editor and L. Meinert, the *Economic Geology* editor.

Financial support was provided by CREGU and by the CNR-INSU-CT5 project in 2010. This work was possible thanks to CNRS INSU, the ICEEL CARNOT Institute and

the Lorraine region through the CPER program for the LA-ICP-MS acquisition. This work was done through the national program "Investissement d'avenir" with the reference ANR-10-LABX-21-LabEx RESSOURCES21.

REFERENCES

- Ait Malek, H., Gasquet, D., Bertrand, J.M., and Leterrier, J., 1998, Géochronologie U-Pb sur zircon de granitoïdes éburnéens et panafricains dans les boutonnières protérozoïques d'Igherm, du Kerdous et du Bas Draa (Anti-Atlas occidental, Maroc): *Comptes Rendus de l'Académie des Sciences, Paris*, v. 327, p. 819–826.
- Aquilina, L., Boulvais, P., and Mossman, J.R., 2011, Fluid migration at the basement/sediment interface along the margin of the South-East basin (France): Implications for Pb-Zn ore formation: *Mineralium Deposita*, v. 46, p. 959–979.
- Bakker, R.J., 1997, CLATHRATES: Computer programs to calculate fluid inclusion: V–X. Properties using clathrate melting temperatures: *Computer Geosciences*, v. 23, p. 1–18.
- 2003, Package FLUIDS 1. Computer programs for analysis of fluid inclusion data and for modelling bulk fluid properties: *Chemical Geology*, v. 194, p. 3–23.
- Banks, D.A., and Yardley, B.W.D., 1992, Crush-leach analysis of fluid inclusions in small natural and synthetic samples: *Geochimica et Cosmochimica Acta*, v. 56, p. 245–248.
- Banks, D.A., Davies, G.R., Yardley, B.W.D., McCaig, A.M., and Grant, N.T., 1991, The chemistry of brines from an Alpine thrust system in the Central Pyrenees: An application of fluid inclusion analysis to the study of fluid behaviour in orogenesis: *Geochimica et Cosmochimica Acta*, v. 55, p. 1021–1030.
- Baroudi, Z., Beraaouz, E.L. H., Rahimi, A., Saquaque, A., and Chouhaidi, M.Y., 1999, Minéralisations polymétalliques argentifères d'Imiter (Jbel Saghro, Anti-Atlas, Maroc): *Minéralogie, évolution des fluides et mécanismes de dépôt: Chronique de la Recherche Minière*, v. 536–537, p. 91–112.
- Barrett, T.J., and Anderson, G.M., 1982, The solubility of sphalerite and galena in NaCl brines: *Economic Geology*, v. 77, p. 1923–1933.
- 1988, The solubility of sphalerite and galena in 1–5 m NaCl solutions at 300°C: *Geochimica et Cosmochimica Acta*, v. 52, p. 813–820.
- Benchekroun, F., and Essarraj, S., 2015, Modélisation géochimique de la composition du fluide argentifère du gisement d'argent d'Imiter (Anti-Atlas, Maroc): 9^{ème} colloque international «Magmatisme, Métamorphisme et Minéralisations Associées» 3MA 2015, Agadir-Tatouant, Morocco (2–4 April, 2015).
- Benharref, M., 1991, Le Précambrien de la boutonnière d'El Kelâa des Mgouna (Saghro, Anti-Atlas, Maroc). *Pétrographie et structure de l'ensemble, implications lithostratigraphiques et géodynamiques*. Ph.D. thesis, Marrakesh, Morocco, Cadi Ayyad University.
- Bodnar, R.J., 1993, Revised equation and table for determining the freezing point depression of H₂O-NaCl solutions: *Geochimica et Cosmochimica Acta*, v. 57, p. 683–684.
- Bohlke, J.K., and Irwin, J.J., 1992, Laser microprobe analyses of noble gas isotopes and halogens in fluid inclusions: Analyses of microstandards and synthetic inclusions in quartz: *Geochimica et Cosmochimica Acta*, v. 56, p. 187–201.
- Boiron, M.C., Essarraj, S., Sellier, E., Cathelineau, M., Lespinasse, M., Poty, B., 1992, Identification of fluid inclusions in relation to their host microstructural domains in quartz by cathodoluminescence: *Geochimica et Cosmochimica Acta*, v. 56, p. 175–185.
- Boiron, M.C., Cathelineau, M., Banks, D.A., Buschaert, S., Fourcade, S., Coulbaly, Y., Boyce, A., and Michelot, J.L., 2002, Fluid transfers at the basement/cover interface. Part II: Large-scale introduction of chlorine into the basement by Mesozoic brines: *Chemical Geology*, v. 192, p. 121–140.
- Boiron, M.C., Cathelineau, M., and Richard, A., 2010, Fluid flows and metal deposition near basement/cover unconformity: lessons and analogies from Pb-Zn-F-Ba systems for the understanding of Proterozoic U deposits: *Geo-fluids*, v. 10, p. 270–292.
- Borisenko, A.S., Borovikov, A.A., Pavlova, G.G., Kalinin, Yu.A., Nevolko, P.A., Gushchina, L.V., Lebedev, V.I., Maacha, L., and Kostin, A.V., 2013, Formation conditions of Hg-silver deposition at the Imiter deposit (Anti-Atlas, Morocco): *Biennial SGA Meeting, 12th, 2013, Uppsala, Sweden, Proceedings*, v. 3.
- Borisenko, A.S., Lebedev, V.I., Borovikov, A.A., Pavlova, G.G., Kalinin, Yu. A., Nevolko, P.A., Maacha, L., and Kostin, A.V., 2014, Forming conditions and age of native silver deposits in Anti-Atlas (Morocco): *Doklady Earth Sciences*, v. 456, pt. 2, p. 663–666.
- Bouch, J.E., Naden, J., Shepherd, T.J., McKerverey, J.A., Young, B., Benham, A.J., and Sloane, H.J., 2006, Direct evidence of fluid mixing in the formation of stratabound Pb-Zn-Ba-F mineralisation in the Alston block, north Pennine orefield (England): *Mineralium Deposita*, v. 41, p. 821–35.
- Bousquet, R., El Mamoun, R., Saddiqi, O., Goffé, B., Möller, A., and Madi, A., 2008, Mélanges and ophiolites during the Pan-African orogeny: The case of the Bou-Azzer ophiolite suite (Morocco): *Geological Society London Special Publications*, v. 297, p. 233–247.
- Bowers, T.S., and Helgeson, H.C., 1983, Calculation of the thermodynamic and geochemical consequences of nonideal mixing in the system H₂O-CO₂-NaCl on phase relations in geologic systems. Equation of state for H₂O-CO₂-NaCl fluids at high pressures and temperatures: *Geochimica et Cosmochimica Acta*, v. 47, p. 1247–1275.
- Bowler, S., 1989, Shape fabric formation by cataclasis in quartz from the Moine thrust zone, northwest Scotland: *Geology*, v. 17, p. 353–356.
- Bucher, K., and Frey, M., 1994, *Petrogenesis of metamorphic rocks*: Berlin, Springer-Verlag, 318 p.
- Burkhard, M., Caritg, S., Helg, U., Robert-Charrue, C., and Soulaïmani, A., 2006, Tectonics of the Anti-Atlas of Morocco: *Comptes Rendus Géosciences*, v. 338, p. 11–24.
- Cathelineau, M., 1988, Cation site occupancy in chlorites and illites as a function of temperature: *Clay Minerals*, v. 23, p. 471–485.
- Cathelineau, M., and Boiron M.C., 2010, Downward penetration and mixing of sedimentary brines and dilute hot waters at 5 km depth in the granite basement at Soultz-sous-Forêts (Rhine graben, France): *Comptes Rendus Géoscience*, v. 342, p. 560–565.
- Cathles, L.M., and Adams, J.J., 2005, Fluid flow and petroleum and mineral resources in the upper (<20 km) continental crust: *Economic Geology 100th Anniversary Volume*, p. 77–110.
- Cheilletz, A., Levresse, G., Gasquet, D., Azizi-Samir, M.R., Zyadi, R., Archibald, A.D., and Farrar, E., 2002, The giant Imiter silver deposit: Neoproterozoic epithermal mineralisation in the Anti-Atlas, Morocco: *Mineralium Deposita*, v. 37, p. 772–781.
- Clauer, N., 1976, *Géochimie isotopique du strontium des milieux sédimentaires. Application à la géochronologie de la couverture du craton ouest-africain*: Ph.D. thesis, France, Strasbourg University, 256 p.
- Clayton, R.N., and Mayeda, T.K., 1963, The use of bromine pentafluoride in the extraction of oxygen from oxides and silicates for isotopic analysis: *Geochimica et Cosmochimica Acta*, v. 27, p. 43–52.
- Crerar, D., Wood, S., and Brantley, S., 1985, Chemical controls on solubility of ore-forming minerals in hydrothermal solutions: *Canadian Mineralogist*, v. 23, p. 333–352.
- Deloule, E., Allegre, C.J., and Doe, B.R., 1986, Lead and sulfur isotope microstratigraphy in galena crystals from Mississippi Valley-type deposits: *Economic Geology*, v. 81, p. 1307–1321.
- Derome, D., Cuney, M., Cathelineau, M., Fabre, C., Dubessy, J., Bruneton, P., and Hubert, A., 2003, A detailed fluid inclusion study in silicified breccias from the Kombolgie sandstones (Northern Territory, Australia): Inferences for the genesis of middle-Proterozoic unconformity-type uranium deposits: *Journal of Geochemical Exploration*, v. 80, p. 259–275.
- Dubessy, J., 1984, Simulation des équilibres chimiques dans le système C-O-H, conséquences méthodologiques pour les inclusions fluides: *Bulletin de Minéralogie*, v. 107, p. 155–168.
- Dubessy, J., Poty, B., and Ramboz, C., 1989, Advances in the C-O-H-N-S fluid geochemistry based on micro-Raman spectroscopic analysis of fluid inclusions: *European Journal of Mineralogy*, v. 1, p. 517–534.
- Dublyansky, Y.V., and Spotl, C., 2009, Hydrogen and oxygen isotopes of water from inclusions in minerals: Design of a new crushing system and on-line continuous-flow isotope ratio mass spectrometric analysis: *Rapid Communications in Mass Spectrometry*, v. 23, p. 2605–2613.
- Ducrot, J., 1979, Datation à 615 Ma de la granodiorite de Bleïda et conséquences sur la chronologie des phases tectoniques, métamorphiques et magmatiques pan-africaines dans l'Anti-Atlas marocain: *Bulletin de la Société Géologique de France*, v. 7, p. 495–499.
- Ducrot, J., and Lancelot, J.R., 1977, Problème de la limite Précambrien-Cambrien. Etude radiochronologique par la méthode U/Pb sur zircons du volcan du Jbel Boho (Anti-Atlas marocain): *Canadian Journal of Earth Sciences*, v. 14, p. 2771–2777.
- El Arabi, E.H., 2007, La série permienne et triasique du rift haut-atlasique: nouvelles datations; évolution tectono-sédimentaire: Ph.D. thesis, Casa-blanca, Morocco, Hassan II University, 225 p.

- Essarraj, S., Boiron, M.C., Cathelineau, M., Banks, D.A., El Boukhari, A., and Chouhaidi, M.Y., 1998, Brines related to Ag deposition in the Zgounder silver deposit (Anti-Atlas, Morocco): *European Journal of Mineralogy*, v. 10, p. 1201–1214.
- Essarraj, S., Boiron, M.C., Cathelineau, M., Banks, D.A., and Benharref, M., 2005, Penetration of surface evaporated brines into the Proterozoic basement and deposition of Co and Ag at Bou Azzer (Morocco): Evidence from fluid inclusions: *Journal of African Earth Sciences*, v. 41, p. 25–39.
- Ettaki, M., Ibouh, H., and Chellaï, E., 2007, Les structures diapiriques lia-siques du Haut Atlas central, Maroc: Exemple de la ride d'IKERZI: *Africa Geosciences Review*, v. 14, n° 1, p. 79–93.
- Fontes, J.C., and Matray, J.M., 1993, Geochemistry and origin of formation brines from Paris basin, France. 1: Brines associated with Triassic salts: *Chemical Geology*, v. 109, p. 149–175.
- Frizon de Lamotte, D., Leturmy, P., Missenard, Y., Khomsi, S., Ruiz, G., Saddiqi, O., Michard, A., and Charrière, A., 2009, Meso-Cenozoic vertical movements in the Atlas System (Algeria, Morocco, Tunisia): Origin of longitudinal asymmetry of topography and rock material—an overview: *Tectonophysics*, v. 475, p. 9–28.
- Frizon de Lamotte, D., Zizi, M., Missenard, Y., Hafid, M., El Azzouzi, M., Maury, R.C., Charrière, A., Taki, Z., Benammi, M., and Michard, A., 2008, The Atlas system in Michard, A., Saddiqi, O., Chalouan, A., and Frizon de Lamotte, D., eds., *Continental evolution: The geology of Morocco—structure, stratigraphy, and tectonics of the Africa-Atlantic-Mediterranean Triple Junction*: Berlin Heidelberg, Springer-Verlag p. 133–202.
- Gasquet, D., Levresse, G., Cheillett, A., Azizi-Samir, M.R., and Mouttaqi, A., 2005, Contribution to a geodynamic reconstruction of the Anti-Atlas (Morocco) during Pan-African times with the emphasis on inversion tectonics and metallogenic activity at the Precambrian-Cambrian transition: *Precambrian Research*, v. 140, p. 157–182.
- Gautheron, C., and Moreira, M., 2002, Helium signature of the subcontinental mantle: *Earth Planetary Science Letters*, v. 199, p. 39–47.
- Gilg, H.A., and Sheppard, S.M.F., 1995, Hydrogen isotope fractionation between smectites and water [abs.]: *Terra Abstracts, Abstract Supplement No. 1 to Terra Nova*, v. 7, p. 329.
- Gleeson, S.A., Yardley, B.W.D., Munz, I.A., and Boyce, A.J., 2003, Infiltration of basinal fluids into high-grade basement, South Norway: Sources and behaviour of waters and brines: *Geofluids*, v. 3, p. 33–48.
- Godwin, C.I., Watson, P.H., and Shen, K., 1986, Genesis of the Lass vein system, Beaverdall silver camp, south-central British Columbia: *Canadian Journal of Earth Sciences*, v. 23, p. 1615–1626.
- Graham, D.W., 2002, Noble gas isotope geochemistry of mid-ocean ridge and ocean island basalts: Characterization of mantle source reservoirs, in Porcelli, D., Wieler, R., and Ballentine, C., eds., *Noble gases in geochemistry and cosmochemistry: Reviews in Mineralogy and Geochemistry*, p. 247–318.
- Günther, D., and Heinrich, C.A., 1999, Enhanced sensitivity in laser ablation-ICP mass spectrometry using helium-argon mixtures as aerosol carrier: *Journal of Analytical Atomic Spectrometry*, v. 12, p. 165–170.
- Günther, D., Frischknecht, R., Heinrich, C.A., and Kahlert, H.J., 1997, Capabilities of an argonfluoride 193 nm excimer laser for laser ablation inductively coupled plasma mass spectrometry microanalysis of geological materials: *Journal of Analytical Atomic Spectrometry*, v. 12, p. 939–944.
- Haack, U., Heinrichs, H., Boness, M., and Schneider, A., 1984, Loss of metals from pelites during regional metamorphism: *Contributions to Mineralogy and Petrology*, v. 85, p. 116–132.
- Hammerli, J., Rusk, B., Spandler, C., Emsbo, P., and Oliver, N.H.S., 2013, In situ quantification of Br and Cl in minerals and fluid inclusions by LA-ICP-MS: A powerful tool to identify fluid sources: *Chemical Geology*, v. 337–338, p. 75–87.
- Hammerli, J., Spandler, C., Oliver, N.H.S., and Rusk, B., 2014, Cl/Br of scapolite as a fluid tracer in the earth's crust: Insights into fluid sources in the Mary Kathleen fold belt, Mt. Isa inlier, Australia: *Journal of Metamorphic Geology*, v. 32, p. 93–112.
- Hammerli, J., Spandler, C., Oliver, N.H.S., Sossi, P., and Dipple, G.M., 2015, Zn and Pb mobility during metamorphism of sedimentary rocks and potential implications for some base metal deposits: *Mineralium Deposita*, v. 50, no. 6, p. 657–664, DOI 10.1007/s00126-015-0600-5.
- Hejlen, W., Muchez, P., Banks, D.A., Schneider J., Kucha, H., and Keppens, E., 2003, Carbonate-hosted Zn-Pb deposits in Upper Silesia, Poland: Origin and evolution of mineralizing fluids and constraints on genetic models: *Economic Geology*, v. 98, p. 911–932.
- Hemley, J.J., Cygan, G.L., Fein, J.B., Robinson, G.R., and D'Angelo, W.M., 1992, Hydrothermal ore-forming processes in the light of studies in rock-buffered systems: 1. Iron-copper-zinc-lead sulfide solubility relations: *Economic Geology*, v. 87, p. 1–22.
- Holser, A.W.T., 1979, Trace elements and isotopes in evaporates: *Reviews in Mineralogy*, v. 6, p. 295–346.
- Huon, S., Cornée, J.J., Piqué, A., Raïs, N., Clauer, N., Liewig, N., and Zayane, R., 1993, Mise en évidence au Maroc d'événements thermiques d'âge triasico-liasique liés à l'ouverture de l'Atlantique: *Bulletin de la Société Géologique de France*, v. 164, p. 165–176.
- Huyck, H.L.O., 1991, When is a metalliferous black shale not a black shale?: *U.S. Geological Survey Circular 1058*, p. 42–56.
- Inglis, J.D., MacLean, J.S., Samson, S.D., D'Lemos, R.S., Admou, H., and Hefferan, K., 2004, A precise U-Pb zircon age for the Bleida granodiorite, Anti-Atlas, Morocco: Implications for the timing of deformation and terrane assembly in the eastern Anti-Atlas: *Journal of African Earth Sciences*, v. 39, p. 277–283.
- Kendrick, M.A., Burgess, R., Leach, D., and Patrick, R.A.D., 2002, Hydrothermal fluid origins in Mississippi Valley-type ore districts: Combined noble gas (He, Ar, K) and halogen (Cl, Br, I) analysis of fluid inclusions from the Illinois-Kentucky fluorspar district, Viburnum Trend, and Tri-State districts, midcontinent United States: *Economic Geology*, v. 97, p. 453–469.
- Knauth, L.P., and Beeunas M.A., 1986, Isotope geochemistry of fluid inclusions in Permian halite with implications for the isotope history of ocean water and the origin of saline formation waters: *Geochimica et Cosmochimica Acta*, v. 50, p. 419–433.
- Knipe, S.W., Foster, R.P., and Stanley, C.J., 1991, Hydrothermal precipitation of precious metals on sulfide substrates, in Ladeira, E.A., ed., *Brazil Gold 91*: Rotterdam, Balkema, p. 431–435.
- 1992, The role of sulfide surfaces in the sorption of precious metals from hydrothermal fluids: *Transactions of the Institution of Mining and Metallurgy*, v. 101, p. 83–88.
- Kyser, K., Hiatt, E., Renac, C., Durocher, K., Holk, G., and Deckart, K., 2000, Diagenetic fluids in Paleo- and Meso-Proterozoic sedimentary basins and their implications for long protracted fluid histories: *Mineralogical Association of Canada, Short course*, v. 28, p. 225–262.
- Laville, E., and Piqué A., 1991, La distension crustale atlantique et atlasique au Maroc au début du Mésozoïque: Le rejet des structures hercyniennes: *Bulletin de la Société Géologique de France*, v. 162, p. 1161–1171.
- Leach, D.L., Viets, J.B., Foley-Ayuso, N., and Klein, D.P., 1995, Mississippi Valley-type Pb-Zn deposits: *U.S. Geological Survey Open-File Book 95-831*.
- Leach, D.L., Marsh, E., Emsbo, P., Rombach, C.S., Kelley, K.D., and Anthony, M., 2004, Nature of hydrothermal fluids at the shale-hosted Red Dog Zn-Pb-Ag deposits, Brooks Range, Alaska: *Economic Geology*, v. 99, p. 1449–1480.
- Leach, D.L., Sangster, D.F., Kelley, K.D., Large, R.R., Garven, G., Allen, C.R., Gutzmer, J., and Walters, S., 2005, Sediment-hosted lead-zinc deposits: A global perspective: *Economic Geology 100th Anniversary Volume*, p. 561–607.
- Lebedev, V.I. 1998, Ore-magmatic systems of typical arsenide cobalt deposits: Novosibirsk, SB RAS Press (in Russian).
- Lebedev, V.I., and Nagaytsev, Y.V., 1980, Minor elements in metamorphic rocks as an ore-metal source for certain deposits: *Geochemistry International*, v. 17, p. 31–40.
- Leblanc, M., 1972, Sur le style disharmonique des plis hercyniens de la couverture, dans l'Anti-Atlas central (Maroc): *Comptes Rendus de l'Académie des Sciences, Paris*, v. 275, p. 803–806.
- Leblanc, M., and Lbouabi, M., 1988, Native silver mineralisation along a rodingite tectonic contact between serpentinite and quartz-diorite (Bou Azzer, Morocco): *Economic Geology*, v. 83, p. 1379–1391.
- Leisen, M., 2011, Analyse chimique des inclusions fluides par ablation laser couplée à l'ICP-MS et applications géochimiques: Ph.D. thesis, Nancy-France, University of Lorraine, 306 p.
- Leisen, M., Dubessy, J., Boiron, M.C., and Lach P., 2012a, Improvement of the determination of element concentrations in quartz-hosted fluid inclusions by LA-ICP-MS and Pitzer thermodynamic modeling of ice melting temperature: *Geochimica et Cosmochimica Acta*, v. 90, p. 110–125.
- Leisen, M., Boiron M.C., Richard A., Dubessy J., 2012b, Determination of Cl and Br concentrations in individual fluid inclusions by combining microthermometry and LA-ICPMS analysis: Implications for the origin of salinity in crustal fluids: *Chemical Geology*, v. 330–331, p. 197–206.

- Leisen, M., Boiron, M.C., Essarraj, S., and Dubessy, J., 2013, Origin of brines associated with the Bou Azzer silver deposit, Anti-Atlas, Morocco: A LA-ICPMS study of Individual fluid inclusions [abs.]: *Goldschmidt 2013 Conference Abstracts*, p. 1582.
- Leistel, J.M., and Qadrouci, A., 1991, Le gisement argentifère d'Imiter (protérozoïque supérieur de l'Anti-Atlas, Maroc). Contrôles des minéralisations, hypothèse génétique et perspectives pour l'exploration: *Chronique de la Recherche Minière*, v. 505, p. 5–22.
- Levesse, G., 2001, Contribution à l'établissement d'un modèle génétique des gisements d'Imiter (Ag-Hg), Bou Madine (Pb-Zn-Cu-Ag-Au) et Bou Azzer (Co-Ni-As-Au-Ag) dans l'Anti-Atlas marocain: Ph.D. thesis, Nancy, France, Institut National Polytechnique de Lorraine (INPL), 218 p.
- Levesse, G., Cheilletz, A., Gasquet, D., Madi, A., and Ait Haddouch, L., 2001, Existence de minéralisations Co-Ni d'âge Norien (Trias supérieur) à Bou Azzer (anti-Atlas, Maroc): Nouvelles données minéralogiques, géochimiques et géochronologiques: *Magmatisme, Métamorphisme et Minéralisation Associées 3MA, Marrakesh, Morocco, Proceedings*.
- Levesse, G., Cheilletz, A., Gasquet, D., Reisberg, L., Deloule, E., Marty, B., and Kyser, K., 2004, Osmium, sulphur and helium isotopic results from the giant Neoproterozoic epithermal Imiter silver deposit, Morocco: Evidence for a mantle source: *Chemical Geology*, v. 207, p. 59–79.
- Longerich, H.P., Jackson, S.E., and Günther, D., 1996, Laser ablation inductively coupled plasma mass spectrometric transient signal data acquisition and analyte concentration calculation: *Journal of Analytical Atomic Spectrometry*, v. 11, p. 899–904.
- Marshall, D.D., Diamond, L.W., and Skippen, G.B., 1993, Silver transport and deposition at Cobalt, Ontario, Canada: Fluid inclusion evidence: *Economic Geology*, v. 88, p. 837–854.
- Mathieu, R., Cuney, M., and Cathelineau, M., 2000, Evolution of P-T-X conditions around the Oklo reaction zones: *Journal of Geochemical Exploration*, v. 69–70, p. 245–249.
- McCaffrey, M.A., Lazar, B., and Holland, H.D., 1987, The evaporation path of seawater and the coprecipitation of Br⁻ and K⁺ with halite: *Journal of Sedimentary Research*, v. 57, p. 928–937.
- Michard, A., Hoepffner, C., Soulaïmani, A., and Baidder, L., 2008, The Variscan belt, in Michard, A., Saddiqi, O., Chalouan, A., and Frizon de Lamotte, D., eds., *Continental evolution: The geology of Morocco—structure, stratigraphy, and tectonics of the Africa-Atlantic-Mediterranean Triple Junction: Berlin Heidelberg, Springer-Verlag*, p. 65–132.
- Moubiya Mouélé, I., Dudoignon, P., El Albani, A., Meunier, A., Boulvais, P., Gauthier-Lafaye, F., Paquette, J.L., Martin, H., and Cuney, M., 2014, 2.9 to 1.9 Ga paleoalterations of Archean granitic basement of the Franceville basin (Gabon): *Journal of African Earth Sciences*, v. 97, p. 244–260.
- Muchez, P., Heijlen, W., Banks, D.A., Blundell, D., Boni, M., and Grandia, F., 2005, Extensional tectonics and the timing and formation of basin-hosted deposits in Europe: *Ore Geology Reviews*, v. 27, p. 241–67.
- Munz, I.A., Yardley, B.W.D., Banks, D.A., and Wayne, D., 1995, Deep penetration of sedimentary fluids in basement rocks from southern Norway: Evidence from hydrocarbon and brine inclusions in quartz rocks: *Geochimica et Cosmochimica Acta*, v. 59, p. 239–54.
- Nomade, S., Knight, K.B., Beutel, E., Renne, P.R., Verati, C., Féraud, G., Marzoli, A., Youbi, N., and Bertrand, H., 2007, Chronology of the Central Atlantic magmatic province: Implications for the Central Atlantic rifting processes and the Triassic-Jurassic biotic crisis: *Palaeogeography, Palaeoclimatology, Palaeoecology*, v. 244, p. 326–344.
- Oliver, N.H.S., McLellan, J.G., Hobbs, B.E., Cleverley, J.S., Ord, A., and Feltrin, L., 2006, Numerical models of extensional deformation, heat transfer and fluid flow across basement-cover interfaces during basin-related mineralization: *Economic Geology*, v. 101, p. 1–31.
- Ouguir, H., Macaudière, J., Dagallier, G., Qadrouci, A., and Leistel, J., 1994, Cadre structural du gîte Ag-Hg d'Imiter (Anti-Atlas, Maroc): Implication métallogénique: *Bulletin de la Société Géologique de France*, v. 165, p. 233–248.
- Ouguir, H., Macaudière, J., and Dagallier, G., 1996, Le Protérozoïque supérieur d'Imiter, Saghro oriental, Maroc: Un contexte géodynamique d'arrière-arc: *Journal of African Earth Sciences*, v. 22, p. 173–189.
- Oukassou, M., Saddiqi, O., Sebti, S., Michard, A., and Barbarand, J., 2010, Mouvements verticaux dans l'Anti-Atlas (Maroc), apport de la thermochronologie par traces de fission: *Congrès sur la Géologie du Maghreb, 1^{er}, Tlemcen, Algeria, Proceedings*, p. 225–228.
- Ozima, M., and Podosek, F.A., 2002, *Noble gas geochemistry, 2nd ed.*: Cambridge, UK, Cambridge University Press, 286 p.
- Pal'yanova, G., 2008, Physicochemical modeling of the coupled behavior of gold and silver in hydrothermal processes: Gold fineness, Au/Ag ratios and their possible implications: *Chemical Geology*, v. 255, p. 399–413.
- Pasava, J., 1994, Geochemistry and role of anoxic sediments in the origin of the Imiter deposit in Morocco: *Czech Geological Survey Bulletin*, v. 69, p. 1–11.
- Pauwels, H., Fouillac, C., and Fouillac, A.M., 1993, Chemistry and isotopes of deep geothermal saline fluids in the Upper Rhine graben: Origin of compounds and water-rock interactions: *Geochimica et Cosmochimica Acta*, v. 57, p. 2737–2749.
- Pavlova, G.G., Gushchina, L.V., Borovikov, A.A., Borisenko, A.S., and Obolensky, A.A., 2004, Silver and antimony in hydrothermal solutions of Ag-Sb deposits: *Russian Geology and Geophysics*, v. 45, no. 10, p. 1186–1197.
- 2006, Forming conditions for Au-Sb and Ag-Sb ore according to thermodynamic modeling data: *Journal of Material Science*, v. 41, p. 1557–1562.
- Pearce, N.J.G., Perkins, W.T., Westgate, J.A., Gorton, M.P., Jackson, S.E., Nael, C.R., and Chenery, S.P., 1997, Compilation of new and published major trace element data for NIST SRM 610 and NIST SRM 612 glass reference materials: *Geostandards Newsletter*, v. 21, p. 115–144.
- Piqué, A., and Laville, E., 1993, L'ouverture de l'Atlantique central: Un rejeu en extension des structures paléozoïques: *Comptes Rendus de l'Académie des Sciences, Paris*, v. 317, II, p. 1325–1328.
- 1996, The central Atlantic rifting: Reactivation of Palaeozoic structures: *Journal of Geodynamics*, v. 21, p. 235–255.
- Piqué, A., Dahmani, M., Jeannette, D., and Bahi L., 1987, Permanence of structural lines in Morocco from Precambrian to Present: *Journal of African Earth Sciences*, v. 6, no. 3, p. 247–256.
- Piqué, A., Canals, A., Grandia, F., and Banks, D.A., 2008, Mesozoic fluorite veins in NE Spain record regional base metal-rich brine circulation through basin and basement during extensional events: *Chemical Geology*, v. 257, p. 139–152.
- Poisson A., Hadri M., Milhi A., Julien M., and Andrieux J., 1998, The central High Atlas (Morocco). Litho and chrono-stratigraphic correlations during Jurassic times between Tinjdad and Tounfite. Origine of subsidence: *Mémoires du Muséum d'Histoire Naturelle*, v. 179, p. 237–256.
- Poty, B., Leroy, J., and Jachimovicz, L., 1976, Un nouvel appareil pour la mesure des températures sous le microscope: l'installation de la microthermométrie Chaixmeca: *Bulletin de la Société Française de Minéralogie et de Cristallographie*, v. 99, p. 182–186.
- Rais, N., 1992, Caractérisation minéralogique, cristallographique et isotopique d'un métamorphisme polyphasé de faible intensité. Exemple: les grauwackes cambriennes du Maroc occidental: Ph.D. thesis, Brest, France, University of Bretagne Occidentale, 193 p.
- Richard, A., Boulvais, P., Mercadier, J., Boiron, M.C., Cathelineau, M., Cuney, M., and France-Lanord, C., 2013, From evaporated seawater to uranium mineralizing brines: Isotopic and trace element study of quartz dolomite veins in the Athabasca system: *Geochimica et Cosmochimica Acta*, v. 113, 38–59.
- Robert-Charrue, C., and Burkhard, M. 2008, Inversion tectonics, interference pattern and extensional fault-related folding in the eastern Anti-Atlas, Morocco: *Swiss Journal of Geosciences*, v. 101, p. 397–408.
- Russell, M.J., 1978, Downward-excavating hydrothermal cells and Irish-type ore deposits: Importance of an underlying thick Caledonian prism: *Transactions of the Institution of Mining and Metallurgy*, v. 87, p.168–171.
- Sebaï, A., Féraud, G., Bertrand, H., and Hanes, J., 1991, ⁴⁰Ar/³⁹Ar dating and geochemistry of tholeiitic magmatism related to the early opening of the central Atlantic rift: *Earth and Planetary Science Letters*, v. 104, p. 455–472.
- Secor, D.T., Snoko, A.W., and Dallmeyer, R.D., 1986, Character of the Alleghanian orogeny in the southern Appalachians: Part III. Regional tectonic relations: *Geological Society of America Bulletin*, v. 97, p. 1345–1353.
- Shepherd, T.J., 1981, Temperature-programmable, heating-freezing stage for microthermometric analysis of fluid inclusions: *Economic Geology*, v. 76, p. 1244–1247.
- Sheppard, S.M.F., and Gilg, H.A., 1996, Stable isotope geochemistry of clay minerals: *Clay Minerals*, v. 31, p. 1–24.
- Soulaïmani, A., Michard, A., Ouanāmi, H., Baidder, L., Raddi, Y., Saddiqi, O., and Rjimati, E.C., 2014, Late Ediacaran-Cambrian structures and their reactivation during the Variscan and Alpine cycles in the Anti-Atlas (Morocco): *Journal of African Earth Sciences*, v. 98, p. 94–112.
- Steele-MacInnis, M., Bodnar, R.J., and Naden, J., 2011, Numerical model to determine the composition of H₂O-NaCl-CaCl₂ fluid inclusions based on microthermometric and microanalytical data: *Geochimica et Cosmochimica Acta*, v. 75, p. 21–40.

- Stefánsson, A., and Seward, T.M., 2003, Experimental determination of the stability and stoichiometry of sulphide complexes of silver(I) in hydrothermal solutions to 400°C: *Geochimica et Cosmochimica Acta*, v. 67, p. 1395–1413.
- Tarantola, A., Mullis, J., Vennemann, T., Dubessy, J., and de Capitani C., 2007, Oxidation of methane at the CH₄/H₂O-(CO₂) transition zone in the external part of the Central Alps, Switzerland: Evidence from stable isotope investigations: *Chemical Geology*, v. 237, p. 329–357.
- Thiery, R., van den Kerkhof, A.M., and Dubessy, J., 1994, vX properties of CH₄-CO₂ and CO₂-N₂ fluid inclusions: Modelling for T, 31°C and P, 400 bar: *European Journal of Mineralogy*, v. 6, p. 753–771.
- Thomas, R.J., Chevallier, L.P., Gresse, P.G., Harmer, R.E., Eglington, B.M., Armstrong, R.A., de Beer, C.H., Martini, J.E.J., de Kock, G.S., Macey, P.H., and Ingram, B.A., 2002, Precambrian evolution of the Sirwa window, Anti-Atlas orogen, Morocco: *Precambrian Research*, v. 118, p. 1–57.
- Tuduri, J., Chauvet, A., Ennaciri, A., and Barbanson, L., 2005, Modèle de formation du gisement d'argent d'Imiter (Anti-Atlas oriental, Maroc). Nouveaux apports de l'analyse structurale et minéralogique: *Comptes Rendus Géosciences*, v. 338, p. 253–261.
- Tullis, J., Christie, J.M., and Griggs, D.T., 1973, Microstructures and preferred orientations of experimentally deformed quartzites: *Geological Society of America Bulletin*, v. 84, p. 297–314.
- Verati, C., Rapaille, C., Féraud, G., Marzoli, A., Marzoli, H., Bertrand, H., and Youbi, N., 2007, Ar-Ar ages and duration of the Central Atlantic magmatic province volcanism in Morocco and Portugal and its relation to the Triassic-Jurassic boundary: *Palaeogeography, Palaeoclimatology, Palaeoecology*, v. 244, p. 308–325.
- Wilkinson, J.J., 2001a, Fluid inclusions in hydrothermal ore deposits: *Lithos*, v. 55, p. 229–272.
- 2010b, A review of fluid inclusion constraints on mineralization in the Irish ore field and implications for the genesis of sediment-hosted Zn-Pb deposits: *Economic Geology*, v. 105, p. 417–442.
- 2014, Sediment-hosted zinc-lead mineralization: Processes and perspectives: *Treatise on Geochemistry*, 2nd ed., v. 13, p. 219–249.
- Yardley, B.W.D., 2005, Metal concentrations in crustal fluids and their relationship to ore formation: *Economic Geology*, v. 100, p. 613–632.
- Yardley, B.W.D., Banks, D.A., and Barnicoat, A.C., 2000, The chemistry of crustal brines: Tracking their origins, *in* Porter, T.M., ed., *Hydrothermal iron oxide copper gold and related deposits, a global perspective*: Townsville, Australian Mineral Foundation, p. 61–70.
- Zheng, Y.F., 1993, Calculation of oxygen isotope fractionation in hydroxyl-bearing silicates: *Earth and Planetary Science Letters*, v. 120, p. 247–263.
- 1999, Oxygen isotope fractionation in carbonate and sulfate minerals: *Geochemical Journal*, v. 33, p. 109–126.

